Dependence of Ice Crystal Size Distributions in High Ice Water Content Conditions on Environmental Conditions: Results from the HAIC-HIWC Cayenne Campaign

Yachao Hu[1,2], Greg M. McFarquhar[2,3], Peter Brechner[2,3], Wei Wu[2], Yongjie Huang[3,4], Alexei Korolev[5], Alain Protat[6], Cuong Nguyen[7], Mengistu Wolde[7], Alfons Schwarzenboeck[8], Robert M Rauber[9] and Hongqing Wang[1]

[1]Department of Atmospheric and Oceanic Sciences, School of Physics, Peking University, Beijing, China

[2]Cooperative Institute for Severe and High Impact Weather Research and Operations, University of Oklahoma, Norman, Oklahoma, USA

[3]School of Meteorology, University of Oklahoma, Norman, Oklahoma, USA

[4]Center for Analysis and Prediction of Storms (CAPS), University of Oklahoma, Norman, Oklahoma, USA

[5]Environment and Climate Change Canada, Toronto, M3H 5T4, Canada

[6]Australian Bureau of Meteorology, Melbourne, Australia

[7]National Research Council Canada, Ottawa, Canada

[8]Laboratoire de Météorologie Physique, UCA, CNRS, Aubière, France

[9]Department of Atmospheric Sciences, University of Illinois at Urbana-Champaign, Urbana, IL, USA

*Corresponding Author:

Greg McFarquhar

Cooperative Institute for Severe and High Impact Weather Research and Operations, University of Oklahoma

120 David L. Boren Blvd, Suite 2100

Norman, OK 73072

Email: mcfarq@ou.edu

Abstract

A new method that automatically determines the modality of an observed particle size distribution (*PSD*) and the representation of each mode as a gamma function was used to characterize data obtained during the High Altitude Ice Crystals and High Ice Water Content (HAIC-HIWC) project based out of Cayenne, French Guiana in 2015. *PSDs* measured by a 2-D stereo probe and a precipitation imaging probe for particles with maximum dimension (D_{max}) > 55 μm were used to show how the gamma parameters varied with environmental conditions, including temperature (*T*) and convective properties such as cloud type, mesoscale convective system (MCS) age, distance away from the nearest convective peak, and underlying surface characteristics. Four kinds of modality *PSDs* were observed, unimodal *PSDs* and three types of multimodal *PSDs* (Bimodal1 with breakpoints 100 ± 20 μm between modes, Bimodal2 with breakpoints 1000 ± 300 μm and Trimodal *PSDs* with two breakpoints). The *T* and Ice Water Content (*IWC*) are the most important factors influencing the modality of *PSDs*, with the frequency of multimodal *PSDs* increasing with increasing *T* and *IWC*. An ellipsoid of equally plausible solutions in (N_o-λ-μ) phase space is defined for each mode of the observed *PSDs* for different environmental conditions. The percentage overlap between ellipsoids was used to quantify the differences between overlapping ellipsoids for varying conditions. The volumes of the ellipsoid decrease with increasing *IWC* for most cases, and (N_o-λ-μ) vary with environmental conditions related to distribution of *IWC.* HIWC regions are dominated by small irregular ice crystals and columns. The parameters (N_o-λ-μ) in each mode exhibit mutual dependence.

1. Introduction

Cirrus covers 20–30% of the Earth (Heymsfield and McFarquhar, 2002; Wylie et al., 2005), and affects the vertical profile of radiative heating (e.g., Ackerman et al., 1988). Anvil cirrus shields produced when convective ice detrains into the upper troposphere can significantly impact the atmosphere's radiation budget (e.g., Machado and Rossow, 1993; Fu et al., 1995; Zender and Kiehl, 1997; Del Genio and Kovari, 2002; Stephens, 2005). The size, shape, and concentration of ice particles in cirrus have a large impact on cloud radiative forcing, and hence determine cloud feedbacks that modify estimates of global climate change (Ackerman et al., 1988; Mitchell et al., 2008; Sanderson et al., 2008; Lawson et al., 2010). In addition, ice microphysical properties are of particular importance due to the strong sensitivity of simulated deep convective systems to parameterizations of microphysical process rates (Chen and Cotton, 1988; McCumber et al., 1991; Gilmore et al., 2004; Milbrandt and Yau, 2005; McFarquhar et al., 2006; Morrison and Grabowski, 2008; Huang et al., 2020) that depend on the habits and size distributions of ice crystals.

The number distribution function [$N(D)$] of ice crystals determines many microphysical properties (e.g., ice water content *IWC*, total number concentration N_t, mass-weighted terminal velocity v_m, effective radius R_e, bulk extinction β, and single scattering properties), parameterizations of which are important for the Earth system models (e.g., Stephens, 2005; Jakob and Klein, 1999; Sanderson et al., 2008; Jackson et al., 2015) and weather models (e.g., Morrison et al., 2009; Bryan and Morrison, 2012; Stanford et al., 2019) because they control distributions of latent heating and cooling, condensate loading and radiant fluxes (Schlimme et al., 2005) that are directly coupled with model dynamics (Morrison et al., 2015). Mass-weighted terminal velocity determined by particle size distributions (*PSDs*) controls the cloud coverage and lifetime simulated by climate models (Sanderson et al., 2008), and impacts spatial distributions of latent heating by affecting microphysical process rates (i.e., riming aggregation, melting, evaporation, etc.). Further, the accuracy of cirrus remote sensing retrievals depends on accurate representations of *PSDs* (Wolf et al., 2019). The effective diameter (D_e) depends on *PSDs* and is commonly used to parameterize single scattering properties needed for calculation of shortwave radiative transfer (e.g., Fu, 1996; McFarquhar and Heymsfield, 1998; Mitchell, 2002). The radar reflectivity is a higher-order moment of *PSDs* in the Rayleigh scattering regime

(Smith, 1984). Thus, correct interpretation of ice crystal *PSDs* is critically needed for development and evaluation of model parameterization schemes and remote sensing retrievals (Gu et al., 2011).

Many microphysical parameterization schemes, such as the Milbrandt 2-moment scheme (Milbrandt and Yau, 2005), the Thompson scheme (Thompson et al., 2008), the State University of New York at Stony Brook scheme by Yanluan Lin (SBU-YLIN; Lin and Colle, 2011), and the predicted particle properties (P3) scheme (Morrison and Milbrandt, 2015) make assumptions about the number and type of categories of the hydrometeors present and the shape of the *PSDs* in each category. A plethora of studies found considerable sensitivity of high-resolution numerical weather prediction forecasts to the selection of the microphysics schemes and the use of parameters in such schemes (e.g., Wang, 2002; McFarquhar et al., 2006; 2012; Zhu and Zhang, 2006; Li and Pu, 2008; Van Weverberg et al., 2011; Clark et al., 2012; Huang et al., 2020).

PSDs have been fit using exponential or gamma functions in many parameterization schemes (e.g., Walko et al., 1995; Meyers et al., 1997; Straka and Mansell, 2005; Milbrandt and Yau, 2005). The gamma function used to represent the number distribution function $N(D_{max})$ is typically represented by

$$N(D_{max}) = N_o\ D_{max}^{\mu} e^{-\lambda D_{max}}. \quad (1)$$

with N_o the intercept, D_{max} the maximum crystal dimension, λ the slope, and μ the dispersion parameter (e.g., Gilmore et al., 2004; Straka and Mansell, 2005; Milbrandt and Yau, 2005; Moisseev and Chandrasekar, 2007; Wolf et al., 2019; Chen et al., 2020). However, the units of N_o vary with μ in Eq. (1). Thus, the gamma function can alternately be written

$$N(D_{max}) = N_o\ (\frac{D_{max}}{D_o})^{\mu} e^{-\lambda D_{max}}. \quad (2)$$

where D_o = 1 cm is frequently assumed so that N_o has identical units to $N(D_{max})$ (cm^{-3} μm^{-1} or m^{-4}; McFarquhar et al., 2015; Mascio et al., 2020).

Knowledge about the dependence of N_o, λ and μ on environmental conditions is important, because such parameters affect the simulation of cloud properties (e.g., McCumber et al., 1991; McFarquhar et al., 2006). Many in-situ observations have been used to fit the measured *PSDs* (e.g., Gunn and Marshall, 1958; Wong et al., 1988; Heymsfield et al., 2002, 2009; McFarquhar and Black, 2004; McFarquhar et al., 2007) by different techniques to minimize the difference between the observed *PSDs* and fitted *N(D)*. For example, the least squares method (e.g., McFarquhar and Heymsfield, 1997), the method of moments (e.g., Field, 2005; Smith and Kliche, 2005; Smith et al., 2009; Tian et al., 2010; Handwerker and Straub, 2011), and the maximum-likelihood approach (e.g., Haddad et al., 1996) have all been used. Sometimes uncertainty has been taken into account when estimating the fit parameters for observed *PSDs* to improve the fitting techniques (e.g., Wong and Chidambaram, 1985; Chandrasekar and Bringi, 1987; Moisseev and Chandrasekar, 2007; Smith et al., 2009; Handwerker and Straub, 2011). McFarquhar et al. (2015) developed an Incomplete Gamma Fitting (IGF) Technique that uses statistical uncertainty and variability in microphysical properties within a family of distributions to represent the fit parameters as an ellipsoid of equally realizable solutions in (N_o, λ and μ) phase space. The results showed that N_o, λ and μ exhibited some mutual dependence, which must be accounted for when applying the results of the fits.

This technique has been used to study how the ellipsoids describing gamma distributions vary with environmental conditions (e.g., Mascio et al., 2020) and complement other studies showing how the most likely fit parameters vary with environmental conditions (e.g., Thompson et al., 2008; Tian et al., 2010). However, these studies did not consider the multimodal properties of *PSDs* even though previous studies showed two peaks in measured *PSDs* (e.g., Varley, 1978; Mitchell et al., 1996; McFarquhar and Heymsfield, 1997; Jensen et al., 2009; Zhao et al., 2010; Lawson et al., 2010). Breakpoints between these peaks or between the two modes in the *PSDs* sometimes occurred at a size near the cutoff between two instruments used to measure the *PSDs* (e.g., McFarquhar and Heymsfield, 1997; Zhao et al., 2010), but also frequently occurred at sizes not near the cutoff between instruments (e.g., Jackson et al., 2015). Further, peaks and breakpoints were also found in *PSDs* measured by only one probe (e.g., Mitchell et al., 1996; Jensen et al., 2009). Attempts to parameterize multimodal size distributions include those by Welch et al. (1980) who used two modified gamma distribution and Jackson et al. (2015) who extended the McFarquhar et al. (2015) IGF technique to allow for a bimodal gamma distribution function. Although these studies improved the understanding on the distribution of ice crystals, sufficient data were not yet available to characterize the *PSDs* from tropical zones and high *IWC* regions.

The High Altitude Ice Crystals (HAIC; Dezitter et al., 2013) and High Ice Water Content (HIWC; Strapp et al., 2016a) projects collected airborne in-situ and remote sensing data from large oceanic convective clouds, with the primary objective of collecting a dataset of high IWC measurements for assessment of a new aircraft certification envelope for the ice crystal environment (Strapp et al., 2021). Campaigns were performed using the French Falcon-20 out of Darwin, Australia in 2014 (Leroy et al., 2017) and Cayenne, French Guiana in 2015 (Dezitter et al., 2013; Strapp et al., 2016a), whereas the HIWC-RADAR flight campaign out of Florida in 2015 (Yost et al., 2018, Ratvasky et al., 2019) used the NASA DC-8. The HAIC-HIWC data provide a wealth of in-cloud microphysical measurements that have been used to investigate HIWC regions (e.g., Protat et al., 2016; Wolde et al., 2016; Fontaine et al., 2017; Leroy et al., 2016a, 2016b, 2017; Qu et al., 2018; Yost et al., 2018; Huang et al., 2021). For example, a companion study (Hu et al., 2021) investigated the dependence of *IWC* and median mass diameter (*MMD)* on environmental conditions (e.g., temperature, vertical velocity, underlying surface characteristics defined as whether the surface was land, ocean or coastline, mesoscale convective system (MCS) age, the distance away from the convective core and the local strength of convection) for data obtained from the Cayenne field campaign.

Brechner (2021) developed a new method that automatically identifies the existence of up to three peaks in *PSD*s, integrating each mode over all crystal sizes rather than having an artificial breakpoint between modes for *PSDs* as done by Jackson et al. (2015). Brechner's (2021) method was used to investigate the nature of *PSD*s measured during the first phase of the HAIC-HIWC field campaign collected in Darwin, Australia in 2014. The analysis of data collected during the second HAIC-HIWC campaign field conducted from 9-29 May 2015 out of Cayenne, French Guiana presented in Hu et al. (2021) is extended here to quantitatively describe the dependence of *PSDs* on *IWC* and environmental conditions.

The remainder of this paper is organized as follows. Section 2 describes the HAIC-HIWC dataset and methodology used to process the data. Section 3 presents a case study on the nature of different modality *PSDs*. Investigations of how statistical distributions of *PSDs* parameters vary with environmental conditions are shown in section 4. Section 5 summarizes the significance of this study and offers directions for future research.

2. Data and Methodology

a. Overview of campaign

The second HAIC-HIWC flight campaign based out of Cayenne (French Guiana) 9-29 May 2015 collected in-situ and remotely sensed data of oceanic convective clouds to characterize and improve the understanding of the high altitude and high concentration ice crystal environment. A total of 17 French Falcon-20 flights and 10 Canadian National Research Council (NRC) Convair-580 flights are used here. The Convair-580 did almost all of its sampling at levels corresponding to T of approximately −10 °C due to its limited ceiling. The French Falcon-20, equipped with in-situ cloud probes, conducted 17 flights in oceanic, coastal and continental MCSs at varying levels centered at temperatures of mostly −10, −30, and −45 °C (Strapp et al., 2016a). The temperature refers to the location where the ice particles were measured, but this may not necessarily be the level where they grew. Hu et al. (2021) discussed the flights conducted, the probes used and the procedures by which data were processed. Thus, only a brief summary of the most salient aspects is offered here.

b. In situ probes

Hu et al. (2021) summarized the cloud microphysics probes installed on the Falcon-20. These probes include a Stratton Park Engineering (SPEC, 2011) two-dimension stereo probe (2D-S; nominally sizing diameter (D) between 10–1280 μm), a Droplet Measurement Technologies (DMT, 2009) precipitation image probe (PIP; 100–6400 μm), a DMT Cloud Droplet Probe (CDP-2; 2–49 μm), an isokinetic evaporator probe (IKP2; ~ 0.1–10 g m^{-3} at 200 m s^{-1}) for the primary measurement of bulk total water content TWC (Strapp et al., 2016b), a Science Engineering Associates (SEA) Robust hot wire TWC probe, a Rosemount Icing Detector, and a multi-beam 95 GHz Doppler cloud radar (RAdar SysTem Airborne, RASTA). The Convair-580 was equipped with polarization radar (X and W-band, 9.41 GHz and 94.05 GHz) and a suite of in-situ cloud particle probes, including a 2D-S, a DMT PIP, a DMT CDP-2, an IKP2, where the parameters of these probes are the same as those mounted on Falcon-20. In addition, a Particle Measuring Systems (PMS) Forward Scattering Spectrometer Probe (FSSP-100; 2–47 μm), SPEC Cloud Particle Imager (CPI) with 2.3 μm pixel resolution, were used for further PSD characterization, and an Aventech Aircraft Integrated Meteorological Measurements

System (AIMMS-20) measured temperature, static pressure and wind at the flying levels. Licor hygrometer probes model 6262 and model 840A were used to measure water vapor mixing ratio and calculate relative humidity and ice supersaturation following Korolev and Isaac (2006). More information on the use of these probes for these flight campaigns can be found in Strapp et al. (2020).

c. In situ observations of *PSDs*

Different definitions of particle size have been used to characterize *PSDs*. These include the maximum dimension (D_{max}) (e.g., Mitchell and Arnott, 1994; McFarquhar and Heymsfield, 1996; 1998; McFarquhar and Black 2004; Heymsfield et al., 2013; Jackson et al., 2014; Korolev et al., 2014; Korolev and Field, 2015), the area-equivalent diameter (Locatelli and Hobbs, 1974; Korolev et al., 2014; Waitz et al., 2021), and the mass-equivalent diameter (Seifert and Beheng, 2006). D_{max} is used to characterize particle size because this parameter has been used in most previous studies that examined observed ice particle size distributions. Further parameterizations for mass and terminal fall speed that are used in models are usually formulated in terms of maximum-dimension. Thus, the use of maximum-dimension as opposed to the use of an area-equivalent diameter ensures self consistency in model schemes (McFarquhar and Black, 2004). There are several different ways that D_{max} has been calculated for a two-dimensional image (Locatelli and Hobbs, 1974; Brown and Francis, 1995; McFarquhar and Heymsfield, 1996; Mitchell and Arnott, 1994; Korolev and Field, 2015; Heymsfield et al., 2013; Wu and McFarquhar, 2016). The definition of D_{max} as the diameter of a minimum enclosing circle for a two-dimensional particle image is used here following Wu and McFarquhar (2016).

A composite *PSD* was derived from the 2D-S and PIP covering the size range D_{max} from 55 to 12,845 μm at 10 μm resolution and is used to calculate cloud microphysical parameters (e.g., mass concentration distribution, *MMD*, N_t) following the techniques described by Hu et al. (2021). The 2D-S was used in the composite distribution for sizes smaller than 800 μm. Likewise, the PIP was used for sizes larger than 1200 μm, and the composite distribution between 800 and 1200 μm is a linear weighted mean of the 2D-S and PIP distributions (Leroy et al., 2016).

d. Data processing and classifications

Only time periods in ice-phase clouds are examined in this study. Time segments, when the Rosemount Icing Detector frequency was decreasing and was lower than 40 kHz (Mazin et al., 2001) or when N_t measured by the CDP-2 was larger than 10 cm^{-3} (Lance et al., 2010; Ding et al., 2020) identified the presence of liquid water content (*LWC*) and were removed. This represents only 0.81% of the data obtained by Falcon-20 (Hu et al., 2021). A frequency threshold of 39.7 kHz was applied to the different model of the Rosemount Icing Detector installed on the Convair-580 and showed that 24.7% of the data obtained by the Convair-580 was in liquid conditions. To remove tenuous clouds from analysis, only data with $IWC \geq 0.1$ g m^{-3} were used for both aircraft. The HIWC regions were defined to occur when the *IWC* was larger than 1.5 g m^{-3} without any threshold of *MMD* to use a definition consistent with previous studies (e.g., Leroy et al., 2016; Hu et al., 2021). The *IWC* and vertical velocity data were averaged over 5-second intervals to match the integration period used for the *PSD* data. For Falcon-20 flight observations, a total of 12,339 data points representing about 17.2 hours of data within organized MCSs were available for analysis, of which 1,931 data points were in HIWC regions. A total of 6,088 data points representing about 8.5 hours of data within organized MCSs were observed by Convair-580, of which 1,493 data points were in HIWC region.

To investigate the effects of environmental conditions and other MCS characteristics (e.g., temperature, vertical velocity, underlying surface characteristics, MCS age, distance away from the convective core) on *PSDs*, as well as the differences of *PSDs* between HIWC and other *IWC* regions, each measurement was classified according to the several environmental characteristics following the methodology of Hu et al. (2021).

e. Methodology

1) Improved IGF technique

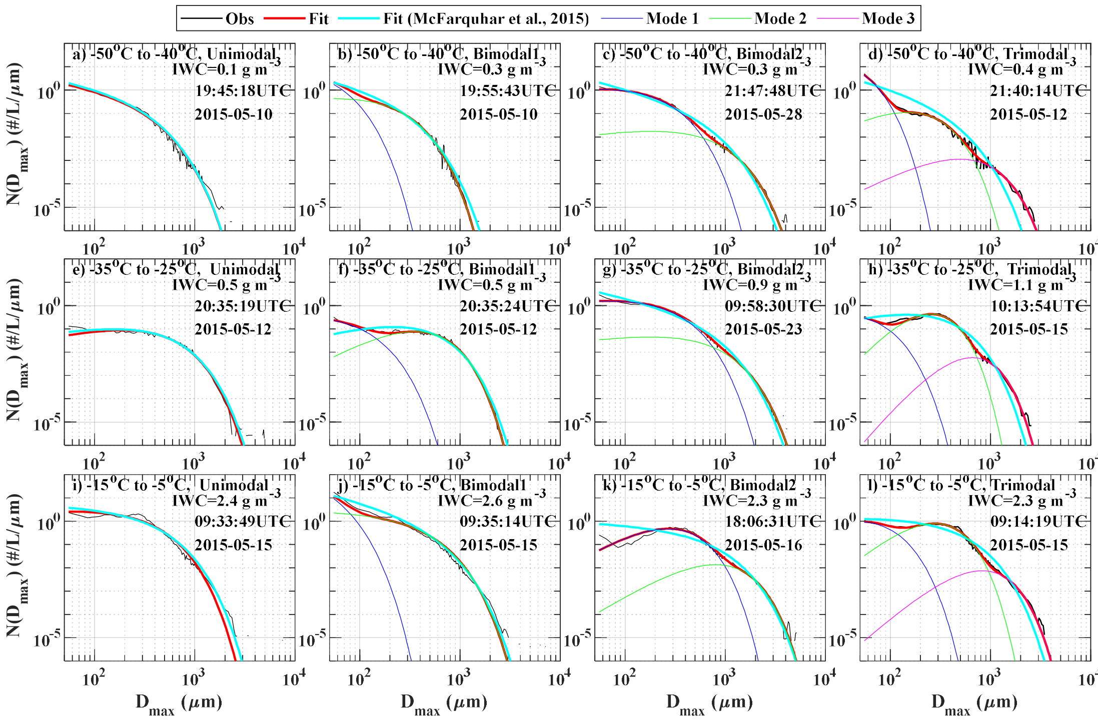

Figure 1. Example of different modality *PSDs* and fits to those *PSDs* as a function of *T* using data obtained during the HAIC-HIWC Cayenne campaign. (a) Unimodal, (b) Bimodal1, (c) Bimodal2, and (d) Trimodal *PSDs* at −50 °C ≤ *T* ≤ −40 °C. (e–h) As Figures 1a–1d but for −35 °C ≤ *T* ≤ −25 °C. (i–l) As Figures 1a–1d but for −15 °C ≤ *T* ≤ −5 °C. Black lines indicate observed *PSDs*, red lines fits to observed *PSD* using method of Brechner (2021) that automatically determines number of modes in *PSDs*, cyan lines represent fit assuming unimodal distribution using the algorithm of McFarquhar et al. (2015), blue, green and pink lines indicate fits to first, second, and third mode of *PSD* respectively.

The algorithm in Brechner (2021) was used to fit the observed *PSDs* to a unimodal, bimodal or trimodal gamma distribution. The algorithm automatically identifies the number of modes and the location of each mode for a *PSD*. The IGF technique developed by McFarquhar et al. (2015) was modified to determine the fit parameters for each mode. To implement the technique, it is first assumed that all *PSDs* are trimodal, with $N(D_{max})$ hence expressed as

$$N(D_{max}) = N_{o1}\left(\frac{D_{max}}{D_o}\right)^{\mu_1} e^{-\lambda_1 D_{max}} + N_{o2}\left(\frac{D_{max}}{D_o}\right)^{\mu_2} e^{-\lambda_2 D_{max}}$$

$$+N_{o3}\left(\frac{D_{max}}{D_o}\right)^{\mu_3} e^{-\lambda_3 D_{max}}. \qquad (6)$$

where the small, middle, and large modes are represented by subscripts (1, 2, 3) respectively. For each *PSD*, a small and large breakpoint is determined. The algorithm determines the number of modes according to the number of breakpoints. If no breakpoint exists, the *PSD* is unimodal and $N_{o2} = N_{o3} = 0$. If two breakpoints exist, the *PSD* is trimodal. If only one breakpoint exists, the *PSD* is bimodal and $N_{o3} = 0$. A breakpoint does not mean that the gamma function for a mode does not characterize crystal sizes larger or smaller, but rather indicates the transition in size at which the dominance of a particular mode changes. Depending on whether the breakpoint is greater 600 μm or less than 200 μm, the bimodal distribution is called Bimodal1 (small breakpoint < 200 μm) or Bimodal2 (large breakpoint > 600 μm). Following McFarquhar et al. (2015), the uncertainty in the number of counts in each size bin was considered in determining the fit to the *PSD*. More details on the development of the scheme are found in Brechner (2021).

Examples of different modality *PSDs* averaged for different temperature (*T*) ranges are shown in Figure 1. The distributions are plotted for different ranges of *T* because *T* is the variable that had the biggest impact on microphysical properties for the Cayenne dataset (Hu et al., 2021). Visually, the fits match the observed *PSDs* well. The shapes of the same modality *PSD* can vary with *T* because the intercept, slope and shape parameters can be a function of *T*. As the generation of particles in different modes is dominated by different processes (small mode by homogeneous nucleation, the large mode by aggregation and sedimentation, and the central mode by riming), the use of three modes should allow better representation of processes in numerical models without the computational expense required by a bin-resolving scheme.

2) Projections of ellipses

An ellipse characterizing the equally realizable solution in (N_o, μ, λ) phase space for each mode was calculated using the algorithm of Moshtagh (2006) that determines a Hessian matrix for the fit phase space for each *PSD*. A restriction of $-1 < \mu < 10$ and $\lambda > 0$ is applied so that the parameterized *PSDs* can easily be integrated when incorporated into model parameterization schemes. To construct a volume of equally realizable solutions for a family of *PSDs* measured in similar environmental conditions, all points contained within 1% of the individual *PSD* ellipsoids in the family are included. The detailed methodology for determining these ellipsoids is found in McFarquhar et al. (2015).

3) Overlap percent

To determine how fit parameters vary with environmental conditions, a three-dimensional volume encompassing two ellipsoids (*S1*, *S2*) describing different environmental conditions is determined (Finlon et al. 2019; Mascio et al. 2020), where $N_{s1,}$ and N_{s2} are the number of points inside the *S1* and *S2* ellipsoids respectively, and N_{s0} is the

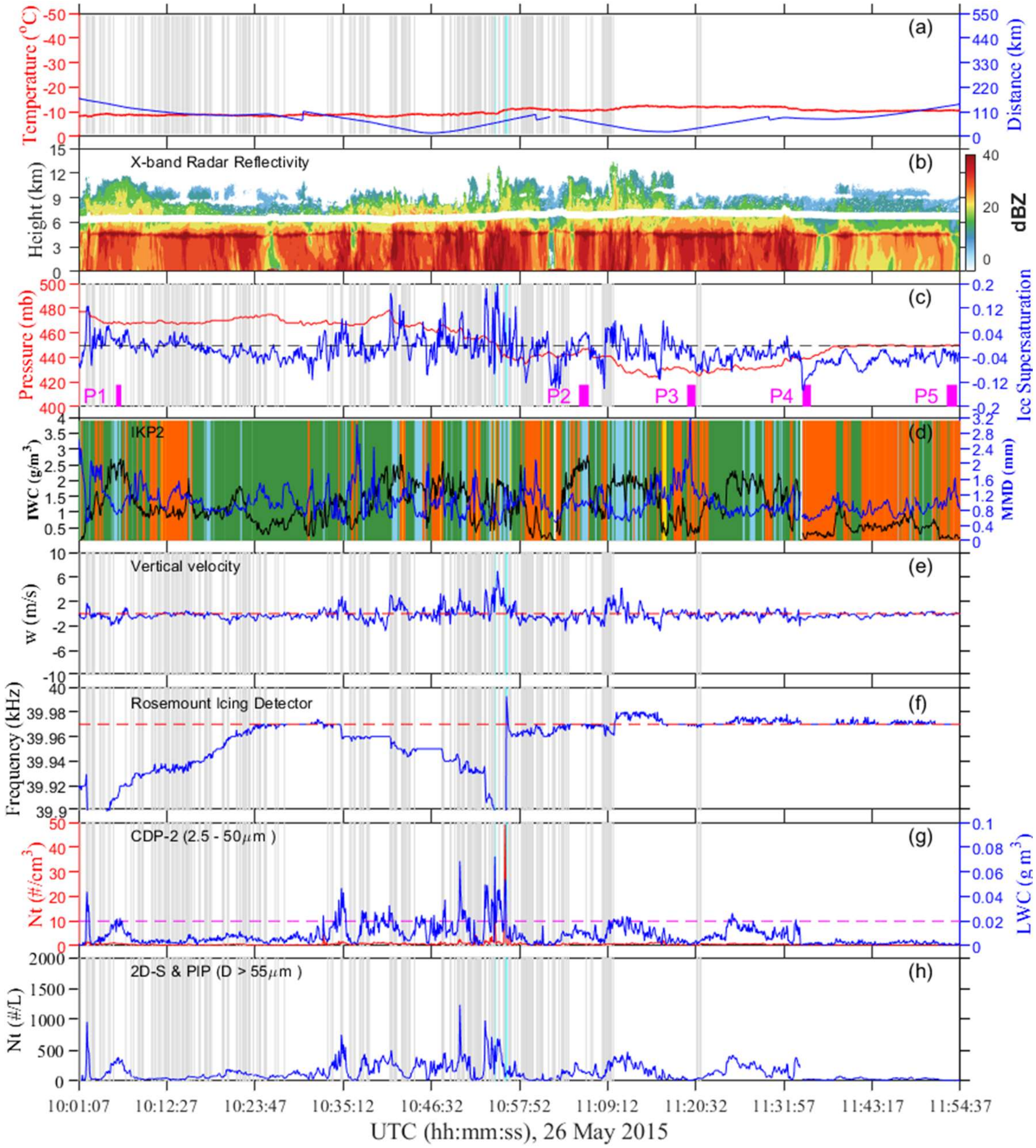

Figure 2. Time series of (a) temperature at flight altitude (red line), distance away from convective core (*L*, blue line, times when aircraft out of MCS not shown); (b) X-band radar reflectivity from X and W-band polarization radar mounted on Convair-580; (c) atmosphere pressure (red line) and ice supersaturation (blue line), with magenta rectangles P1 to P5 representing five periods with their width along x-axis denoting length of time period; (d) *IWC* from IKP2 (black line) and *MMD* (blue line), with

shaded orange boxes representing locations of Unimodal *PSDs*, sky-blue boxes Trimodal *PSDs*, yellow boxes Bimodal1, and green boxes Bimodal2 *PSDs*; (e) vertical velocity (*w*) measured by an Aventech Aircraft Integrated Meteorological Measurements System (AIMMS-20); (f) Rosemount icing detector frequency (blue line) with a threshold of 39.97 kHz indicating presence of supercooled liquid water (red line); (g) N_t (red line) and *LWC* (blue line) derived by integrating $N(D_{max})$ measured by CDP for 2.5 < D_{max} < 50 µm, red line shows threshold of 10 cm^{-3} for N_t used to identify periods of liquid water; and (g) N_t from composite 2D-S (D_{max} > 55 µm) and PIP size distribution for 10:01:07–11:54:37 UTC 26 May 2015 Convair-580 flight leg. Shaded gray boxes represent locations of Rosemount icing detector frequency less than 39.97 kHz, shaded cyan boxes indicated N_t measured by CDP-2 larger than 10 cm^{-3}.

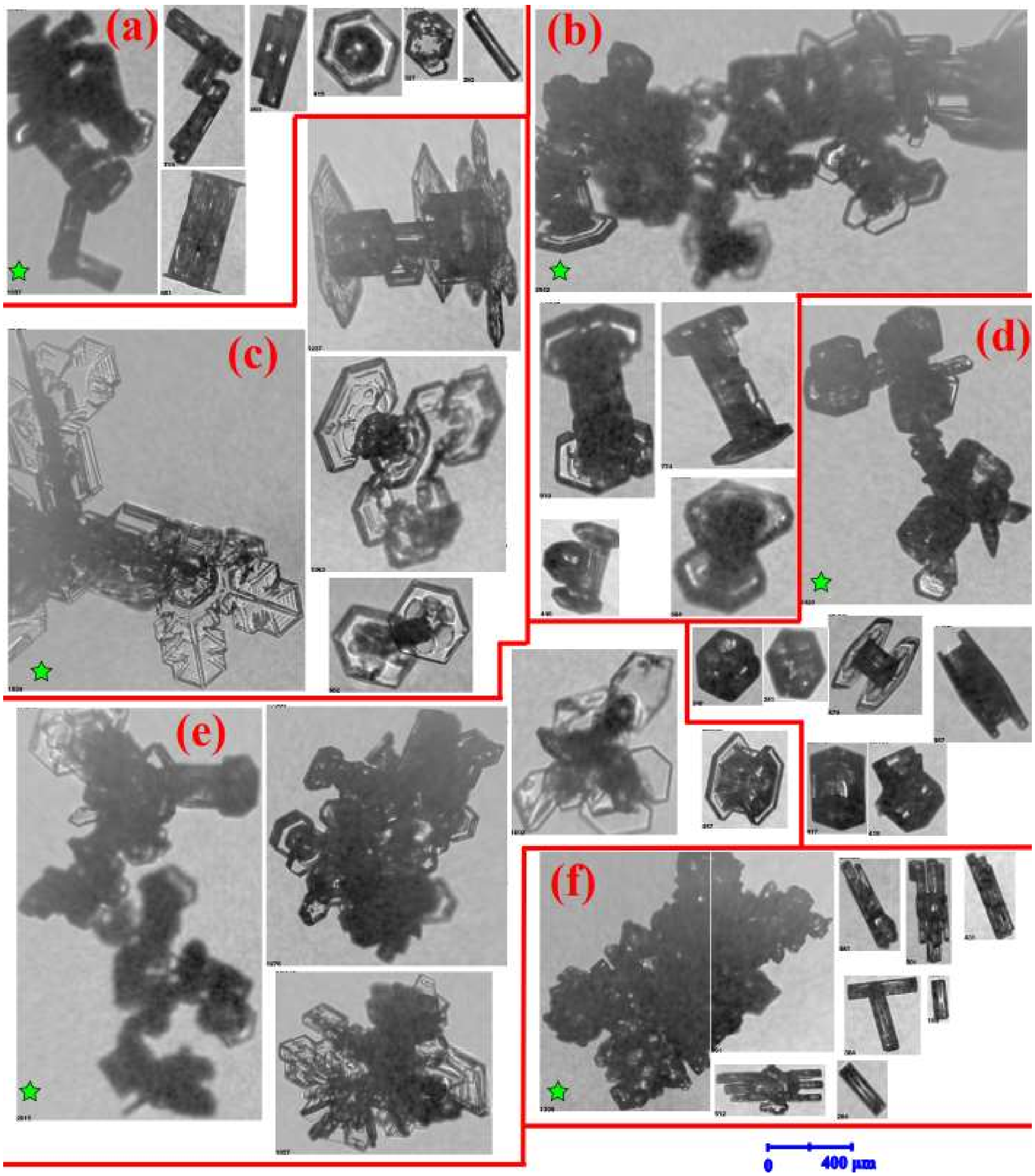

Figure 3. Examples of representative ice crystals measured by SPEC CPI at (a) 10:05:57–10:06:37, (b) 11:05:32–11:06:47, (c) 11:19:27–11:20:32, (d) 11:34:17–11:35:22, and (e) 11:52:52–11:54:12 UTC on

26 May 2015 corresponding to periods P1–P5 in Fig. 2c. (f) Typical ice crystals measured by SPEC CPI 16:08:27–16:09:27 UTC on 26 May 2015. Ice crystal marked by green pentagram of each subgraph means the largest particle of that whole period.

number of points inside both the *S1* and *S2* ellipsoids. The ratio (N_{s0}/N_{s1}) of the equally plausible solutions mean number found in both ellipsoids to the number of points in the *S1* ellipsoid and represents the overlap percent, with (N_{s0}/N_{s2}) representing the same for the *S2* ellipsoid.

3. The distribution of four kinds of modality *PSDs*

a. Case study

Figure 2 shows a time series of microphysical properties measured by probes on the Convair-580 between 10:01:07–11:54:37 UTC on 26 May 2015. The Convair-580 flew at a constant *T* of ~ −10 ºC within an organized Oceanic MCS (Fig. 2a). Representative ice crystals measured by the SPEC CPI shown in Figs. 3(a-e) correspond to P1 (10:05:57–10:06:37), P2 (11:05:32–11:06:47), P3 (11:19:27–11:20:32), P4 (11:34:17–11:35:22), and P5 (11:52:52–11:54:12 UTC) in the morning of 26 May 2015 in Fig. 2c. Typical ice crystals measured by SPEC CPI in Fig. 3f correspond to P6 (16:08:27–16:09:27 UTC; figure not shown) in the afternoon of 26 May 2015. The mean *IWC* and *MMD* are 2.34 g m^{-3} and 738.8 μm respectively during P1, with some columns observed, similar to the ice crystals shapes in Fig. 3f measured during P6, with mean *IWC* and *MMD* are 1.65 g m^{-3} and 432.2 μm respectively. Thus, for this flight small columns dominated the mass content of the *HIWC* regions with small *MMD* (< 500 μm at −10 °C), with some large ice crystals being aggregates of columns. The mean *IWC* reaches 2.53 g m^{-3} during P2 and the mean *MMD* is 959.5 μm, with the large ice crystals being aggregates of columns and plate-like crystals (Fig. 3b). Similar *IWCs* have different *MMD* for P1 and P2, consistent with the larger ice supersaturation in P2 (~ 0.028) compared to P1 (~ 0.008), making the P2 environment more favorable for the growth of ice crystals (Bailey et al., 2009). Besides, the capped column, a column with a plate at either end is observed in P2, suggesting the particle passed through several different growth regimes during its history. The *MMD* reaches 1880 μm when the *IWC* is 0.42 g m^{-3} during P3, consistent with the large crystal with broad branches shown in Fig. 3c. These crystals are typically formed at temperatures around −15 °C at supersaturations greater than those at which plates form. However, ice supersaturation is ~ −0.025 here, consistent with these ice crystals forming in other areas with higher relative humidity condition and falling into this region with transport by the horizontal wind. P4 with low mean *IWC* 0.27 g m^{-3} and *MMD* 597.3 μm, has many small plate crystals (Fig. 3d). Some short and thick capped columns are seen here, different from

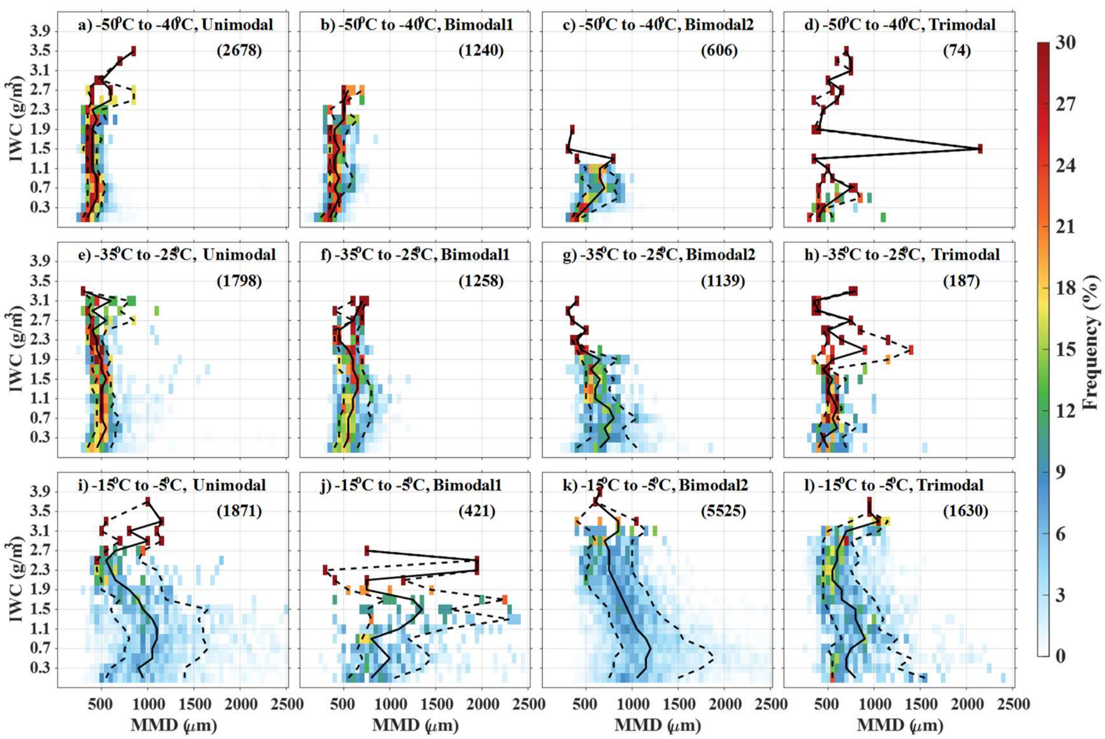

Figure 4. Normalized frequency of *MMD* for each *IWC* range for (a) Unimodal *PSDs*, (b) Bimodal1 *PSDs*, (c) Bimodal2 *PSDs*, and (d) Trimodal *PSDs* for −50 °C ≤ *T* ≤ −40 °C. (e–h) As in Figures 4a–4d but for −35 °C ≤ *T* ≤ −25 °C. (i-l) As in Figures 4a–4d but for −15 °C ≤ *T* ≤ −5 °C. For each subplot, middle solid line indicates 50th percentile, whereas left and right dashed lines represent 15th and 85th *MMD* respectively. Numbers in brackets give numbers of sample data points.

the long and thin capped columns in P2, consistent with the very low ice supersaturations. A region with lower *IWC* (~ 0.21 g m^{-3}) and large *MMD* (~ 1262 μm) found during P5 has plentiful aggregates (Fig. 3e). Many small irregular ice crystals are also found in these six periods. In general, the processes of sedimentation, aggregation, mixing due to shear, vertical wind and horizontal wind transport complicate the analysis because the environment where ice particles are observed does not necessarily represent the environment in which the particles formed or grew. The mixed phase region may also potentially affect the formation of ice crystals. Mixing of air masses with different crystal populations is also very important. Future analysis should try to distinguish between these possibilities by using observations in combination with trajectory analysis and Large Eddy Simulation (LES) modeling studies. HIWC with small *MMD* regions are full of small columns and irregular ice crystals, consistent with a negative correlation between *IWC* and *MMD* (Leroy et al., 2016a; Hu et al., 2021).

Figure 2d shows a time series of *IWC* and *MMD* with the shading indicating the modality of the *PSD*. Trimodal (sky blue) and Bimodal2 *PSDs* (green) occur most frequently in HIWC regions. For example, during P2 when *IWC* > 1.5 g m^{-3}, the modality of *PSDs* is trimodal. When *IWC* decreases to less than 1.5 g m^{-3} at 11:06:57 UTC, the modality becomes Bimodal2 (green) and Unimodal (orange). After 11:09:07 UTC when *IWC* >1.5 g m^{-3}, Trimodal *PSDs* again dominate. A negative correlation coefficient of −0.2 between *IWC* and *MMD* exists for the whole event (1,338 samples, Pearson method, *p-value*: 10^{-13}), consistent with small columns and irregular ice crystals dominating the mass of HIWC regions. Figure 2a shows HIWC regions can be as far away from the convective core as 100 km for the leg at −10 °C (e.g., L > 100 km during P1), suggesting particles were generated in the convective core and then transported and fell into this region (Hu et al., 2021). The lack of response from the Rosemount Icing Detector (Fig. 2f) and the N_t < 10 cm^{-3} measured by the CDP-2 (Fig. 2g) after 11:10:00 UTC confirm that most of these data were collected in ice clouds. However, even though mixed phase regions were excluded from the analysis, many of the ice crystals observed could have formed or grew in mixed-phase regions. N_t measured by the 2D-S and PIP (Fig. 2h) are usually larger for Trimodal *PSDs* (sky blue) and Bimodal2 *PSDs* (green) showing these regions are full of small ice crystals and a positive correlation coefficient of 0.65 between *IWC* and N_t (Pearson method, *p-value*: 10^{-165}) exists during the whole event.

b. Distributions of *MMD* for different modality *PSDs*

To investigate how *MMD* depends on the *PSD* modality, the normalized frequency of *MMD* for each *IWC* range for Unimodal, Bimodal1, Bimodal2, and Trimodal *PSDs* as a function of T is shown in Figure 4. The ranges of *MMD* decrease sharply with decreasing T, consistent with the analysis of Hu et al. (2021). The increase of *MMD* with T is consistent with growth by vapor deposition and aggregation (Mitchell et al., 1996). Increased contributions from sedimentation as larger particles fall to lower altitudes is one of important factors (Jackson et al., 2015). For different modality *PSDs* at the same T, *MMDs* for Bimodal2 and Trimodal *PSDs* are larger than those for Unimodal and Bimodal1 *PSDs* for $T \leq -25$ °C, but trends for -15 °C $\leq T \leq -5$ °C are different. The median *MMD* in Unimodal *PSDs* increases with *IWC* to about 1000 µm at an *IWC* of 1.0 g m^{-3} (Fig. 4i), but sharply decreases thereafter for *IWC* > 1.0 g m^{-3}. Different trends for *MMD* for Bimodal1 and Bimodal2 *PSDs* are seen in Figure 4j and Figure 4k, with *MMD* increasing with *IWC* for Bimodal1 *PSDs* and decreasing for Bimodal2 *PSDs*. The median *MMD* is approximately constant (~ 800 µm) when *IWC* < 1.5 g m^{-3} for Trimodal *PSDs* (Fig. 4l), and *MMD* is the smallest when *IWC* is around 2.3 g m^{-3}. This suggests the number of large ice crystals increases as *IWC* increases for Bimodal1 *PSDs*, and the number of small ice crystals increases as *IWC* increases for other three types of *PSDs*.

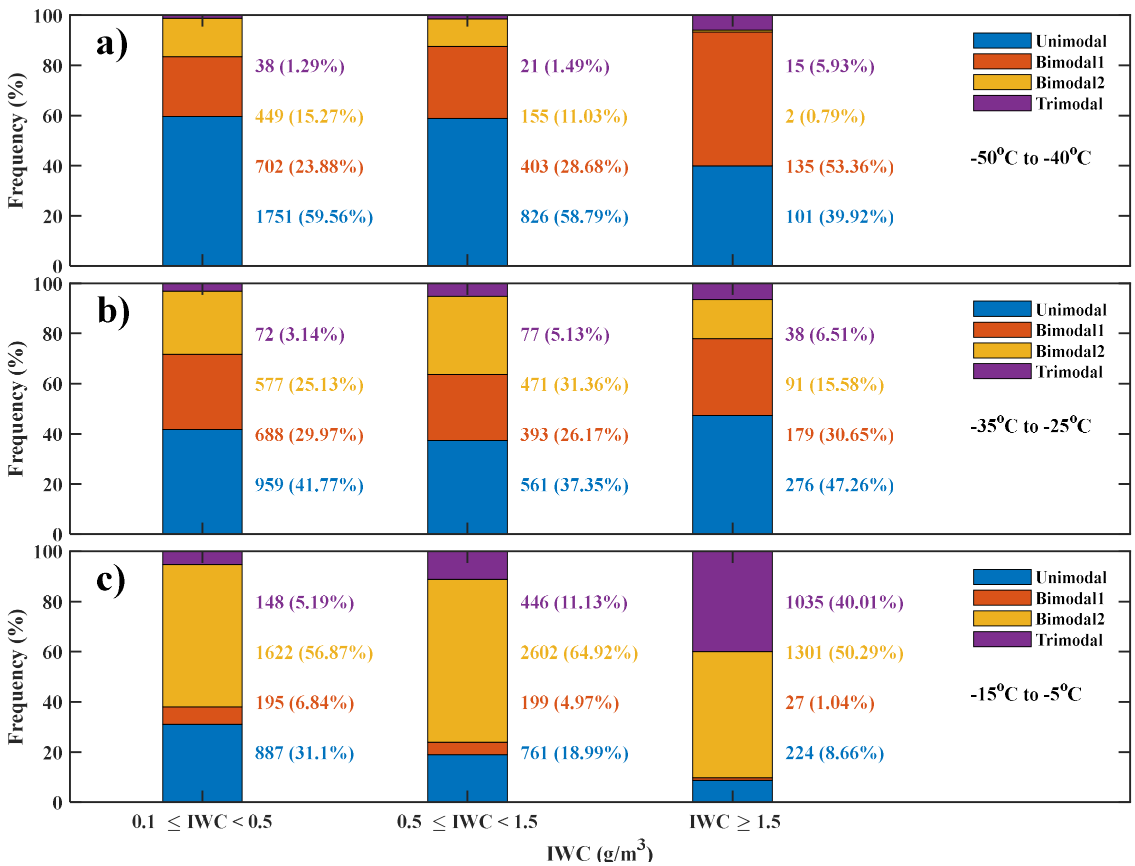

Figure 5. Normalized occurrence frequency of four different modalities determined by Brechner (2021) algorithm for three *IWC* ranges for (a) -50 °C $\leq T \leq -40$ °C, (b) -35 °C $\leq T \leq -25$ °C, and (c) -15 °C $\leq T \leq -5$ °C. Blue represents Unimodal *PSDs*, red Bimodal1 *PSDs*, yellow Bimodal2 *PSDs*, and purple Trimodal *PSDs*. Number of data points and normalized frequency percent (in brackets) of each modality labelled for each *IWC* range in same color as bar. Left column represents 0.1 g m$^{-3} \leq$ *IWC* < 0.5 g m^{-3}, middle 0.5 g m$^{-3} \leq$ *IWC* < 1.5 g m^{-3}, and right *IWC* $\geq$ 1.5 g m^{-3}.

4. *N(D)* as a function of environmental conditions

In this section, the characteristics of the functional fits of the observed *PSDs* are examined as a function of environmental conditions (e.g., cloud types, underlying surface characteristics, MCS ages and distance away from the convective core). As *T* primarily influences the distributions of *IWC* and *MMD* (Hu et al., 2021), *PSDs* were first sorted into three *T* ranges (−15 °C ≤ *T* ≤ −5 °C; −35 °C ≤ *T* ≤ −25 °C; −50 °C ≤ *T* ≤ −40 °C) before examining the influence of other environmental conditions. Most of the data were collected at three different constant altitude legs at *T* of −10, −30, and −45 °C.

a. Different *IWC* regions

To compare *PSDs* in high *IWC* regions with regions without high *IWC*, *PSDs* were sorted into three *IWC*s (0.1 g m^{-3} ≤ *IWC* < 0.5 g m^{-3}, 0.5 g m^{-3} ≤ *IWC* < 1.5 g m^{-3}, *IWC* ≥

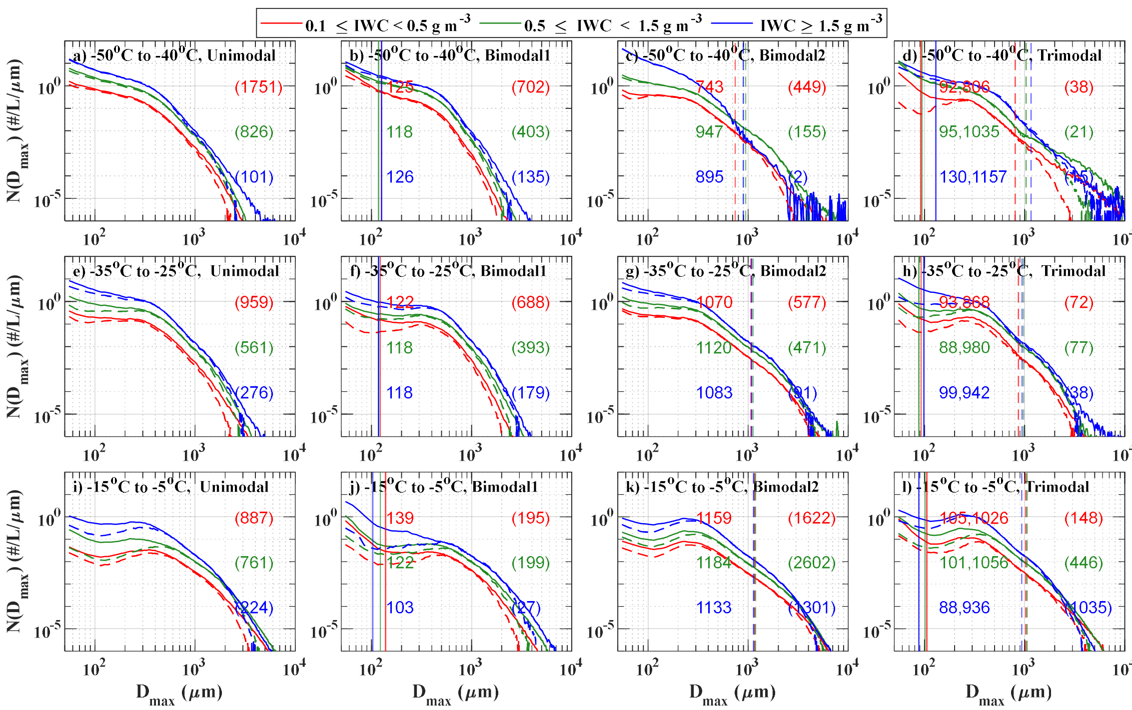

Figure 6. The Mean (solid line) and median (dashed line) distribution of (a) Unimodal, (b) Bimodal1, (c) Bimodal2, and (d) Trimodal *PSDs* for −50 °C ≤ *T* ≤ −40 °C. (e–h) As in Figures 6a–6d but for −35 °C ≤ *T* ≤ −25 °C. (i–l) As in Figures 6a–6d but for −15 °C ≤ *T* ≤ −5 °C. Red lines indicate 0.1 g m^{-3} ≤ *IWC* < 0.5 g m^{-3}, green 0.5 g m^{-3} ≤ *IWC* < 1.5 g m^{-3}, and blue *IWC* ≥ 1.5 g m^{-3}. For multimodal *PSDs*, solid vertical lines represent small breakpoints and dashed lines indicate large breakpoints. Values of breakpoints shown in same color as lines. Numbers in brackets give number of sample data points.

1.5 g m^{-3}). Figure 5 shows the normalized frequency of occurrence of the four different modality *PSDs* for the three *IWC* ranges as a function of *T*. It is apparent that the modality of *PSDs* is strongly dependent on *T* and is related to *IWC*, the frequency of multimodal

PSDs increases with *T*, and the frequency of Unimodal *PSDs* decreases with *T*. For example, the frequency of Unimodal *PSDs* can be larger than 50% for *IWC* < 1.5 g m^{-3} when −50 °C ≤ *T* ≤ −40 °C (Fig. 5a), but decreases to less than 32% when −15 °C ≤ *T* ≤ −5 °C (Fig. 5c). This is consistent with small ice crystals experiencing aggregation when falling from higher to lower altitude, and heterogeneous nucleation in the presence of particles descending from the higher altitude (Zhao et al., 2010), leading to the varying shapes of *PSDs* and frequency of modality of *PSDs* with *T*. The changes of modality with *IWC* are strongly dependent on *T*. For −15 °C ≤ *T* ≤ −5 °C (Fig. 5c), the frequency of Unimodal *PSDs* decreases from ~ 31% to ~ 8.7% with increasing *IWC*, while the frequency of Trimodal *PSDs* increases from ~ 5.2% to ~ 40%. The frequency of Bimodal2 *PSDs*

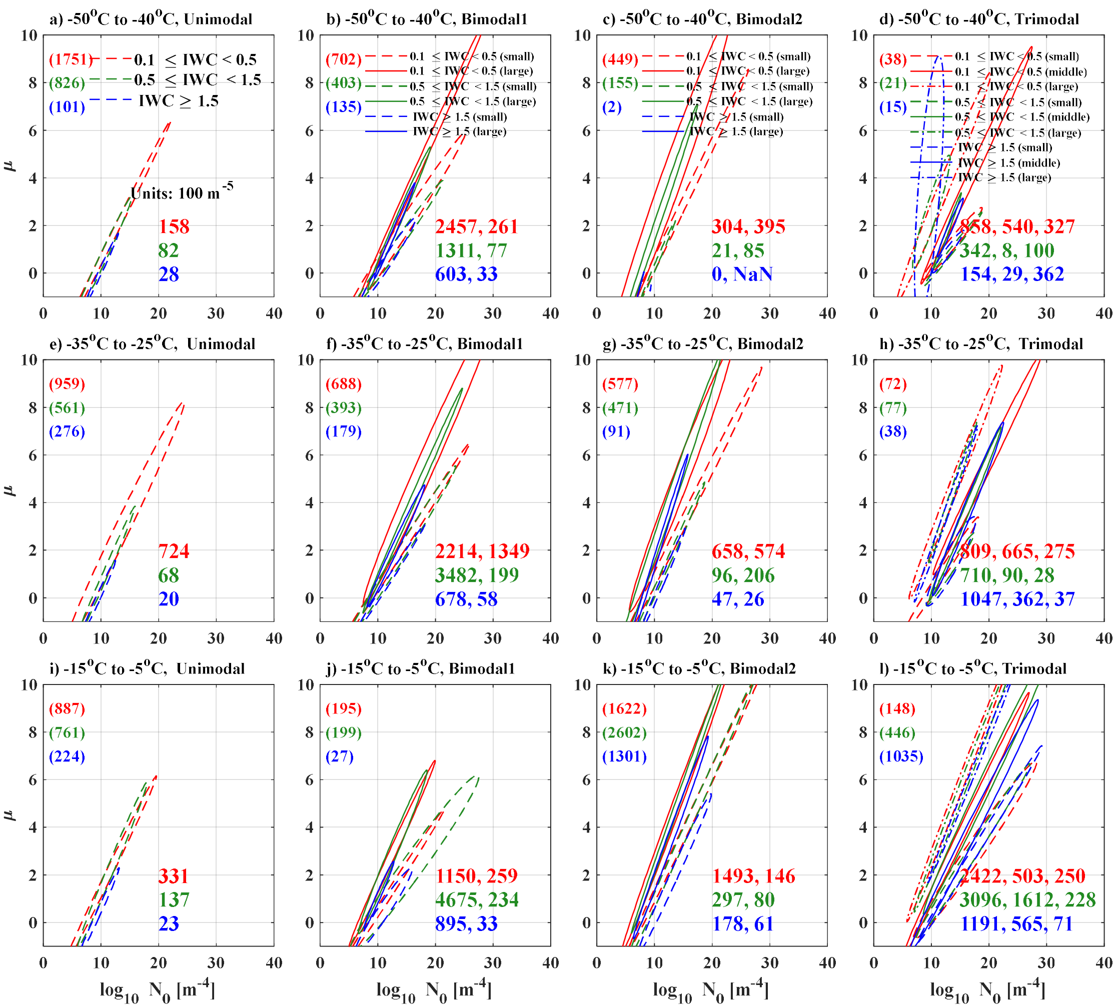

Figure 7. Projection of three-dimensional ellipses characterizing distributions of equally realizable solutions for fit parameters in (N_o, μ) phase space for (a) Unimodal, (b) Bimodal1, (c) Bimodal2, and (d) Trimodal *PSDs* at −50 °C ≤ *T* ≤ −40 °C. (e–h). As Figures 7a–7d but for −35 °C ≤ *T* ≤ −25 °C. (i–l)

As Figures 7a–7d but for −15 °C ≤ *T* ≤ −5 °C. Red lines indicate 0.1 g m^{-3} ≤ *IWC* < 0.5 g m^{-3}, green 0.5 g m^{-3} ≤ *IWC* < 1.5 g m^{-3}, and blue *IWC* ≥ 1.5 g m^{-3}. Different line types represent projections of parameters for different modes in *PSDs*. Numbers in brackets give number of sample data points. The volumes of ellipsoid are denoted by colorful numbers and shown in bottom right corner of each subplot (units: 100 m^{-5}). Unimodal *PSDs* have one column, Bimodal *PSDs* have two columns and three columns for Trimodal *PSDs*. The number of columns from left to right represents the mode from small to large. For each column, top row represents 0.1 g m^{-3} ≤ *IWC* < 0.5 g m^{-3}, middle row 0.5 g m^{-3} ≤ *IWC* < 1.5 g m^{-3}, and bottom row *IWC* ≥ 1.5 g m^{-3}.

increases with increasing *IWC* for −15 °C ≤ *T* ≤ −5 °C, but the frequency of Bimodal1 *PSDs* decreases with increasing *IWC*. However, for −35 °C ≤ *T* ≤ −25 °C and −50 °C ≤ *T* ≤ −40 °C (Figs. 5a and 5b), the frequency of *PSDs* modalities does not show obvious changes with increasing *IWC*. In summary, the frequency of Unimodal *PSDs* decreases and the frequency of multimodal *PSDs* increases with increasing *T*, and different trends for the frequency of the modality of *PSDs* with varying *IWC* for different *T* exist.

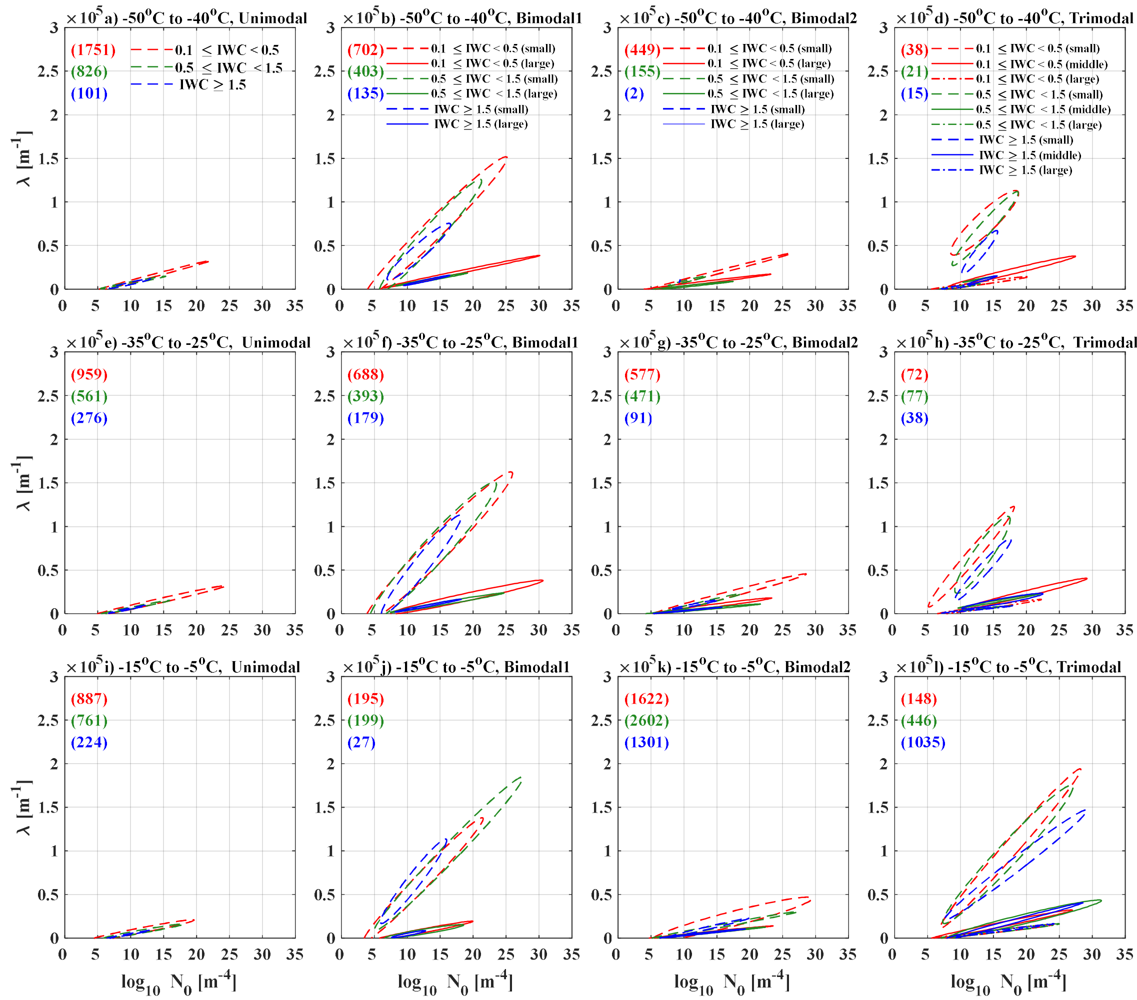

Figure 8. Same as Figure 7 but for (N_o, λ) phase space.

Figure 6 shows the mean (solid line) and median (dashed line) distributions of *PSDs* for different *IWC* regions as a function of T, with breakpoints between modes marked. The shapes of *PSDs* can change a lot even for the same modality with the changes heavily dependent on T. The N_t of small ice crystals (< 200 μm) decreases with increasing T, consistent with *MMD* increases with increasing T and a negative correlation between T and N_t (Jackson et al., 2015; Hu et al., 2021). This is consistent with ice crystals experiencing more aggregation and sedimentation at lower altitudes. Small ice crystals can completely evaporate in subsaturated environments to keep the concentrations of ice crystals with D_{max} < 100 μm relatively low (Korolev et al., 2011, 2013). There are usually more small ice crystals (< 200 μm) and fewer large ice crystals (D_{max} > 2000 μm) as *IWC* increases for Bimodal2 and Trimodal modality at the same T, which is consistent with the *MMD* being negatively correlated with *IWC*. However, for Bimodal1 *PSDs*, the opposite trend can be seen (Figs. 6b, 6f and 6j), as both the number of small and large ice crystals increase with increasing *IWC*, which is consistent with the *MMD* being positively correlated with *IWC* for -15 °C $\leq T \leq -5$ °C (Fig. 4j) and the *MMD* being constant for -35 °C $\leq T \leq -25$ °C and -50 °C $\leq T \leq -40$ °C (Figs. 4b and 4f). The breakpoint between the two modes for Bimodal1 *PSDs* averages 120 ± 20 μm and exhibits little dependence on T. Even though this breakpoint occurs over a size range where the sample volume of the optical array probes is rapidly increasing with particle size (Baumgardner et al., 2017; McFarquhar et al., 2017), the existence of the bimodal distribution does not appear to be instrument related because the bimodal distributions do not occur all the time. The mean breakpoints between the two modes for bimodal2 *PSDs* range between 743 to 1184 μm, with the breakpoints typically increasing with T, and minimal dependence on *IWC*. For the Trimodal *PSDs*, the mean breakpoints between the small mode and middle mode range from 88 to 130 μm, and the mean breakpoints between the middle mode and large mode range from 806 to 1157 μm. The mean breakpoints increase with increasing T for the regions with 0.1 g m^{-3} $\leq$ *IWC* < 0.5 g m^{-3} and decrease with increasing T for the HIWC regions with *IWC* $\geq$ 1.5 g m^{-3}. The small breakpoints and large breakpoints in Trimodal *PSDs* correspond to the breakpoints in the Bimodal1 *PSDs* and the breakpoints in Bimodal2 *PSDs* respectively.

To construct volumes of equally realizable solutions characterizing a family of *PSDs*, McFarquhar et al. (2015) defined a single ellipsoid around all (N_o-λ-μ) contained within at least 1% of the volumes for the *PSDs* contained within a family. The volumes characterizing the different modes in *PSDs* were similarly defined for each mode separately. To visualize the relationship of the gamma fit parameters with *IWC* as a function of *T*, two-dimensional projections of the volumes in (N_o, μ) phase space are shown in Figure 7. Different color lines represent different *IWC* groups, and different types of lines represent the distribution of parameters for the different modes. Regardless of the modality, μ is directly correlated with and increases with N_o. The slopes of the long axis of the ellipse in (N_o, μ) phase space are the largest for the small mode in the Trimodal *PSDs*, while slopes are smallest for the large mode in the Trimodal *PSDs*. The slopes of the long axis of the

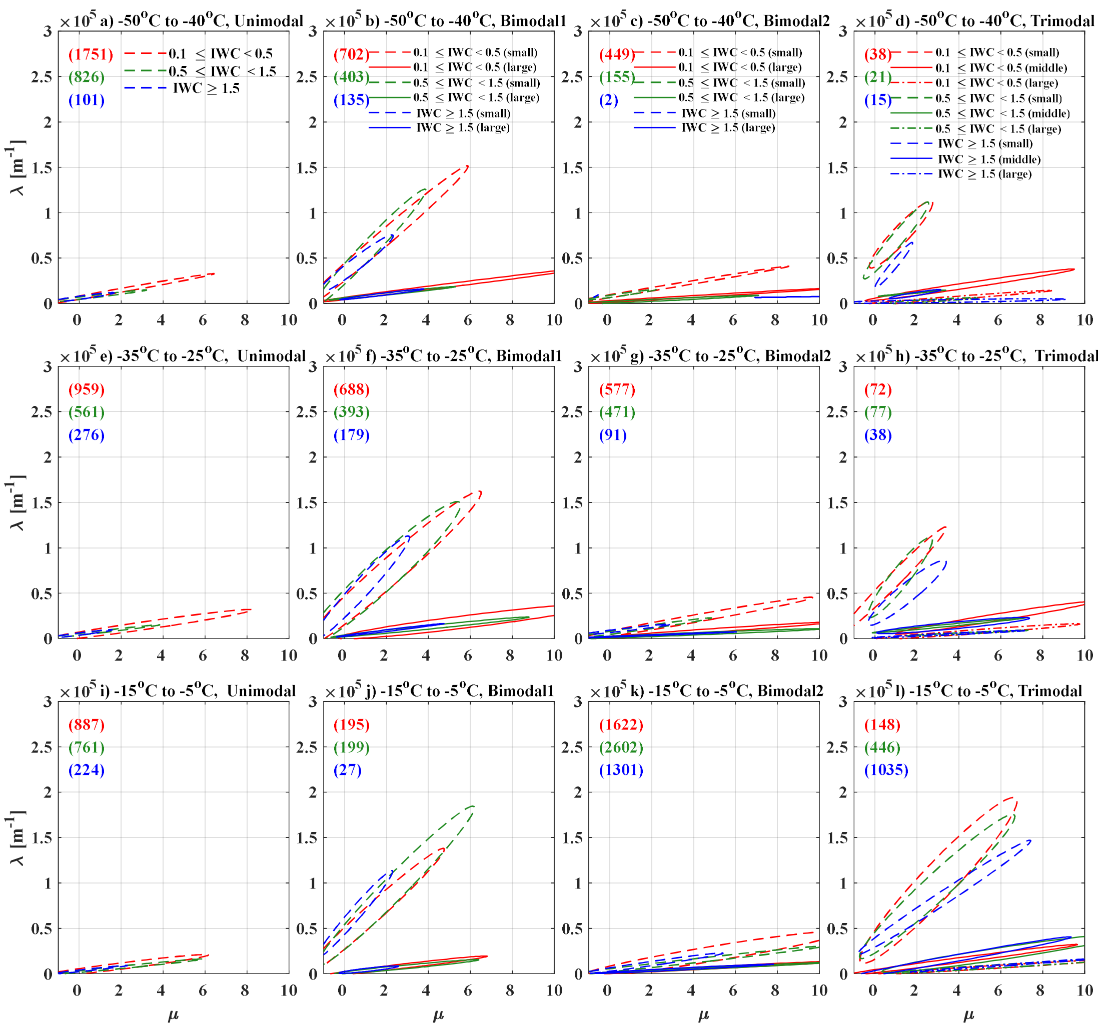

Figure 9. Same as Figure 7 but for (λ, μ) phase space.

ellipse in (N_o, μ) phase space for Bimodal2 are usually larger than those for Bimodal1. In general, the slopes of the long axis of the ellipse in (N_o, μ) phase space in multimodal *PSDs* are larger for the small mode than for the large mode. For the same N_o, μ usually decreases with increasing *IWC*. For example, N_o decreases from 10^{22} m^{-4} to 10^{14} m^{-4} and the maximum of μ decreases from 6.5 to 1.8 for Unimodal *PSDs* for increases in *IWC* from 0.1 g m^{-3} $\leq$ *IWC* < 0.5 g m^{-3} to *IWC* $\geq$ 0.5 g m^{-3} when −50 °C $\leq T \leq$ −40 °C. Consistent with previous findings of Mascio et al. (2020) showing that μ and λ tend to decrease with increasing *IWC*. This means the volumes of ellipses for small *IWC* regions are usually larger than those for large *IWC*. For example, at −50 °C $\leq T \leq$ −40 °C, the volume of ellipsoid for 0.1 g m^{-3} $\leq$ *IWC* < 0.5 g m^{-3} is ~ 1.6×10^{4} m^{-3} μm^{-2}, while it decreased to 2.8 $\times10^{3}$ m^{-3} μm^{-2} when *IWC* > 1.5 g m^{-3}. The smaller μ as *IWC* increases is consistent with more small ice crystals with increasing *IWC*, and with *MMD* decreasing with increasing *IWC*. The range of N_o is from 10^{5} m^{-4} to above 10^{20} m^{-4} values that cover more than 15 orders of magnitude, consistent with previous studies (e.g., McFarquhar et al., 2015; Jackson et al., 2015; Mascio et al.,2020). In addition, these figures also show that there are less prominent impacts on how *T* affects the parameters of *PSDs*.

Figure 8 shows the ellipse distributions in (N_o, λ) phase space for different modes as a function of *T* and *IWC*. Regardless of modality, λ increases with N_o. Similar to (N_o, μ) phase space, the slopes of the long axis of the ellipses in (N_o, λ) phase space are largest for the small mode in Trimodal *PSDs*, and smallest for the large mode in Trimodal *PSDs*. The slopes of the long axis of the ellipse and values of λ in (N_o, λ) phase space for Bimodal1 *PSDs* are usually larger than those in Bimodal2 *PSDs*, due to the existence of more large crystals in the Bimodal2 *PSDs*. This is expected because the breakpoint occurs at a larger D_{max}. For the same N_o, there are less obvious changes for λ with increasing *T* for Unimodal, Bimodal1 and Bimodal2 *PSDs*, while the range of λ increases for the small mode of Trimodal *PSDs*. The range of λ tend to be smaller with increasing *IWC* regardless of the modality of *PSDs* and the ellipses of small *IWCs* are usually larger than those of larger *IWC*s.

Figure 9 shows the ellipse distributions in (μ, λ) phase space. Regardless of modalities, λ increases with increasing μ. Similar to the (N_o, λ) and (N_o, μ) phase spaces, the slopes of the long axis of the ellipse in (μ, λ) phase space are largest for the small mode in the Trimodal *PSDs*, and smallest for the large mode. The slopes of the long axis of the ellipse in (μ, λ) phase space for Bimodal1 *PSDs* are usually larger than those in Bimodal2 *PSDs*. That means for the same μ, λ is usually smaller in Bimodal2 *PSDs* than in Bimodal1 *PSDs*, consistent with the presence of more larger ice crystals in Bimodal2 *PSDs* due to contributions from processes such as aggregation. Similar to the other projections, there is no strong dependence of the slopes of μ and λ on *IWC*, but the volumes of the ellipses of small *IWCs* are usually larger than those of large *IWCs*.

In order to develop a size distribution parameterization for use in models and to learn more about processes occurring in these clouds, it is necessary to quantify the dependence of fit parameters on environmental conditions. Figure 10 shows the fractional

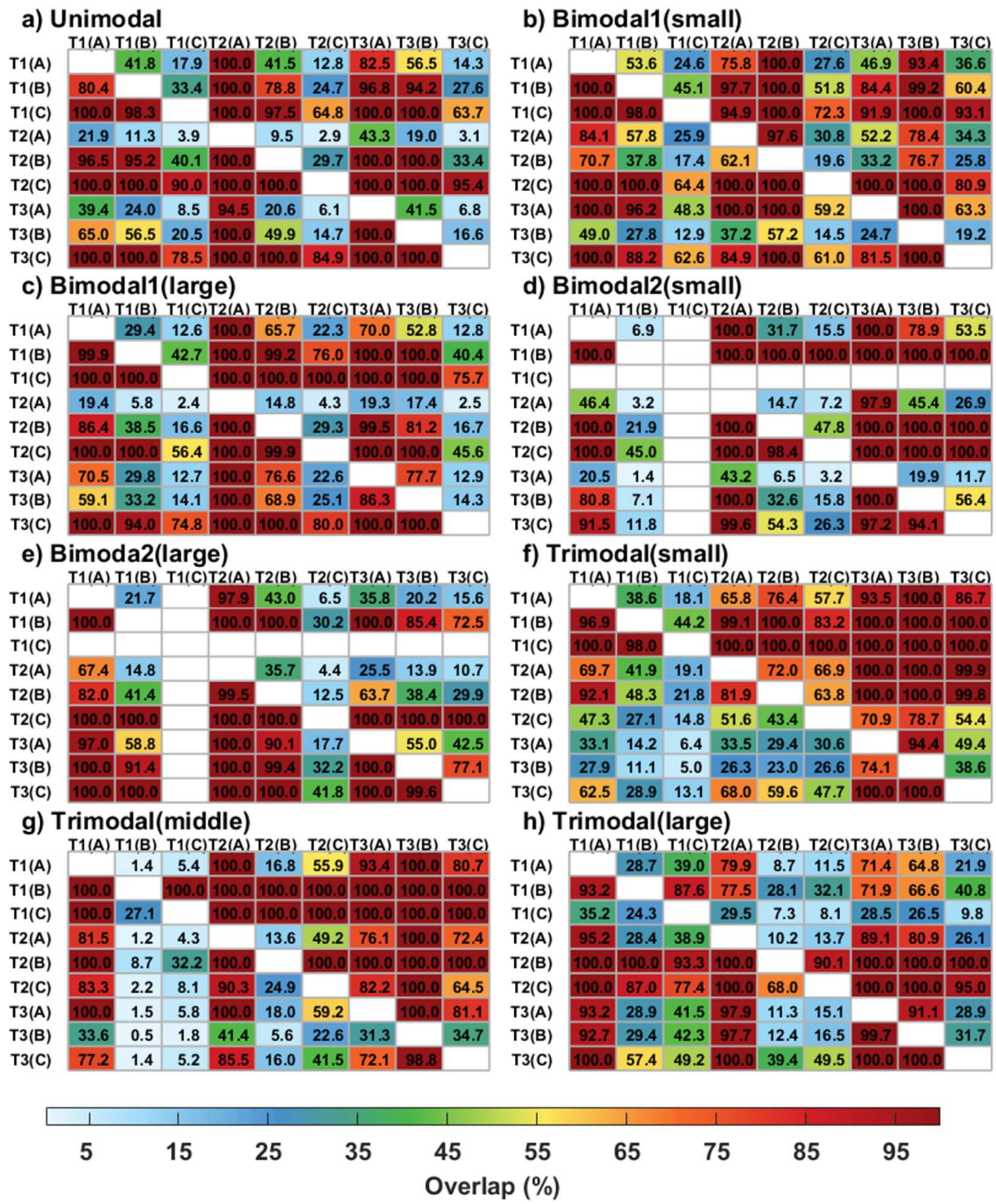

Figure 10. Matrix of percentage overlap between three-dimensional volumes of equally realizable fit parameters for (a) Unimodal, (b) first mode in Bimodal1, (c) second mode in Bimodal1, (d) first mode in Bimodal2, (e) second mode in Bimodal2, (f) first mode in Trimodal, (g) second mode in Trimodal, and (h) third mode in Trimodal *PSDs* as function of *IWC* and *T*. A represents regions with 0.1 g m^{-3} ≤ *IWC* < 0.5 g m^{-3}, B 0.5 g m^{-3} ≤ *IWC* < 1.5 g m^{-3} and C *IWC* ≥ 1.5 g m^{-3}. *T1*, *T2* and *T3* represent −50 °C ≤ *T* ≤ −40 °C, −35 °C ≤ *T* ≤ −25 °C and −15 °C ≤ *T* ≤ −5 °C respectively. Boxes colored according to percent overlap. For example, green box in first row and second column of (a) means 41.8% of the equally plausible solutions found in the −15 °C ≤ *T* ≤ −5 °C and 0.5 g m^{-3} ≤ *IWC* < 1.5 g m^{-3} family are also found in −15 °C ≤ *T* ≤ −5 °C and 0.1 g m^{-3} ≤ *IWC* < 0.5 g m^{-3} family.

overlap between the ellipsoids describing the three-dimensional volumes of equally realizable fit parameters for different *IWC* and *T* ranges for all four modalities. For different

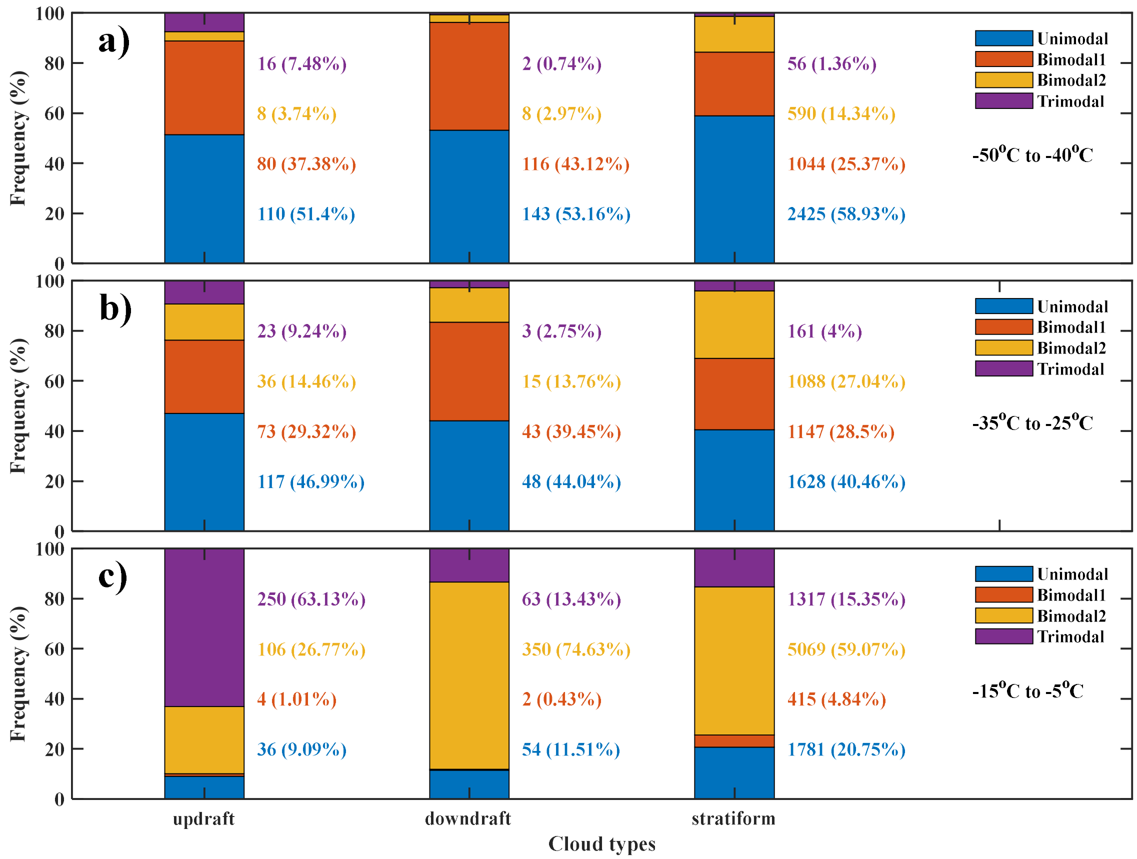

Figure 11. As Figure 5 but for updrafts, downdrafts and stratiform regions.

IWC families at the same *T*, the volumes in regions with $IWC \geq 1.5$ g m^{-3} are usually smaller than the regions with $IWC < 1.5$ g m^{-3} regardless of modality. For example, for the temperature range -15 °C $\leq T \leq -5$ °C the blue box in the first row and third column of figure 10a means 17.9% of the equally plausible solutions with 0.1 g m$^{-3} \leq IWC < 0.5$ g m^{-3} are found in the family with $IWC \geq 1.5$ g m^{-3}, whereas the dark red box in the third row and first column indicates all solutions with $IWC \geq 1.5$ g m^{-3} are contained in the family with 0.1 g m$^{-3} \leq IWC < 0.5$ g m^{-3}. The matrices are not symmetric, because the overlap between any two ellipsoids is unique, and each ellipsoid has its own special central position and range. A prominent feature in Fig. 10a is that for the Unimodal *PSDs* at -15 °C $\leq T \leq -5$ °C, less than 20% of the equally plausible solutions found in regions with $IWC < 1.5$ g m^{-3} are contained in the families with $IWC \geq 1.5$ g m^{-3} while ~ 100% of the points in the family with $IWC \geq 1.5$ g m^{-3} are found in the regions with 0.5 g m$^{-3} \leq IWC < 1.5$ g m^{-3}. Similar trends for volume overlap can be seen for Bimodal1 (small) and Bimodal1 (large). In general, the ellipsoids of 0.1 g m^{-3} ≤ IWC < 0.5 g m^{-3} families have the largest volumes for all modalities, while volumes for IWC ≥ 1.5 g m^{-3} families have the smallest volumes. Except for the large mode in Trimodal *PSDs*, the percent overlap is usually more than 60% and even up to 100% for regions with IWC ≥ 1.5 g m^{-3} when −50 °C ≤ T ≤ −40 °C. This make sense as the volume of ellipsoid for −15 °C ≤ T ≤ −5 °C and IWC ≥ 1.5 g m^{-3} is usually the smallest, consistent with the ranges of parameters shown in Figures 7, 8, and 9, indicating that the parameters (N_o, μ, and λ) are constrained for HIWC regions compared to other regions.

In summary, the volumes of the ellipsoids decrease with increasing IWC because there are more small ice crystals in the higher IWC regions. λ and μ both increase with N_o, and λ increases with increasing μ, consistent with the trends noted by McFarquhar et al. (2007), Heymsfield et al. (2002), and Heymsfield et al. (2013). And, the N_o, λ and μ exhibit mutual dependence and are not truly independent parameters, consistent with previous studies (e.g., McFarquhar et al, 2015; Mascio et al., 2020).

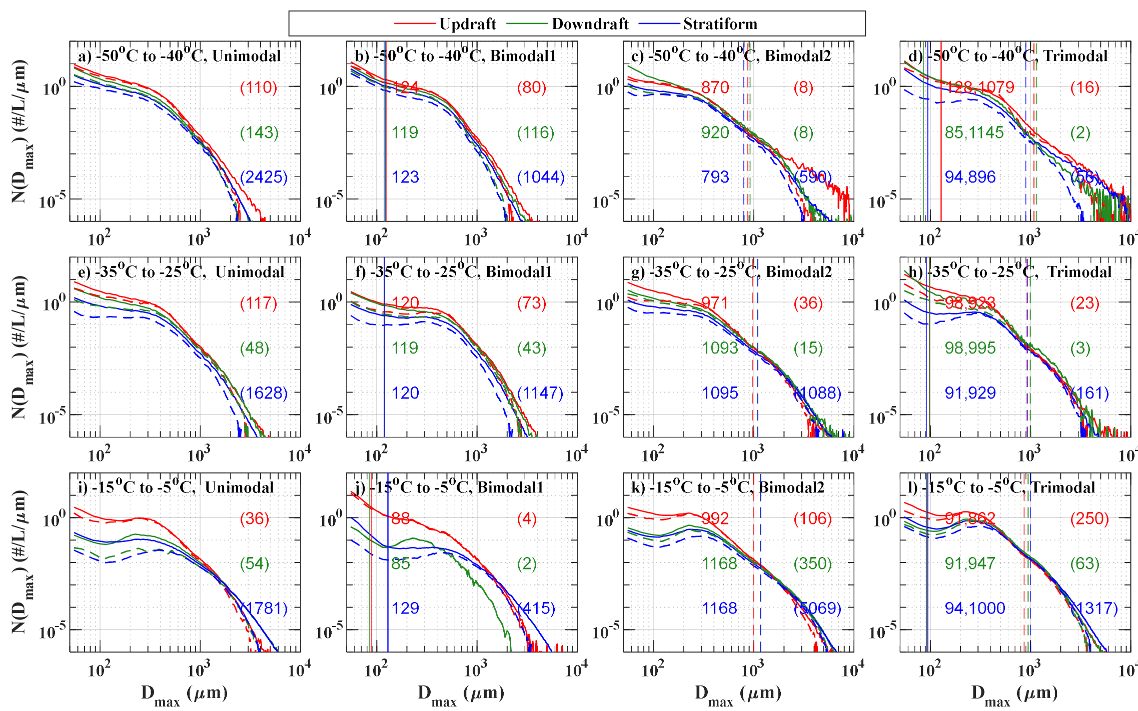

Figure 12. As Figure 6 but segregated according to whether observations obtained in updrafts, downdrafts or stratiform regions.

b. Vertical velocity

To investigate the impact of vertical motion on *PSDs*, data were divided according to whether they were obtained in updrafts, downdrafts, or stratiform regions. A convective

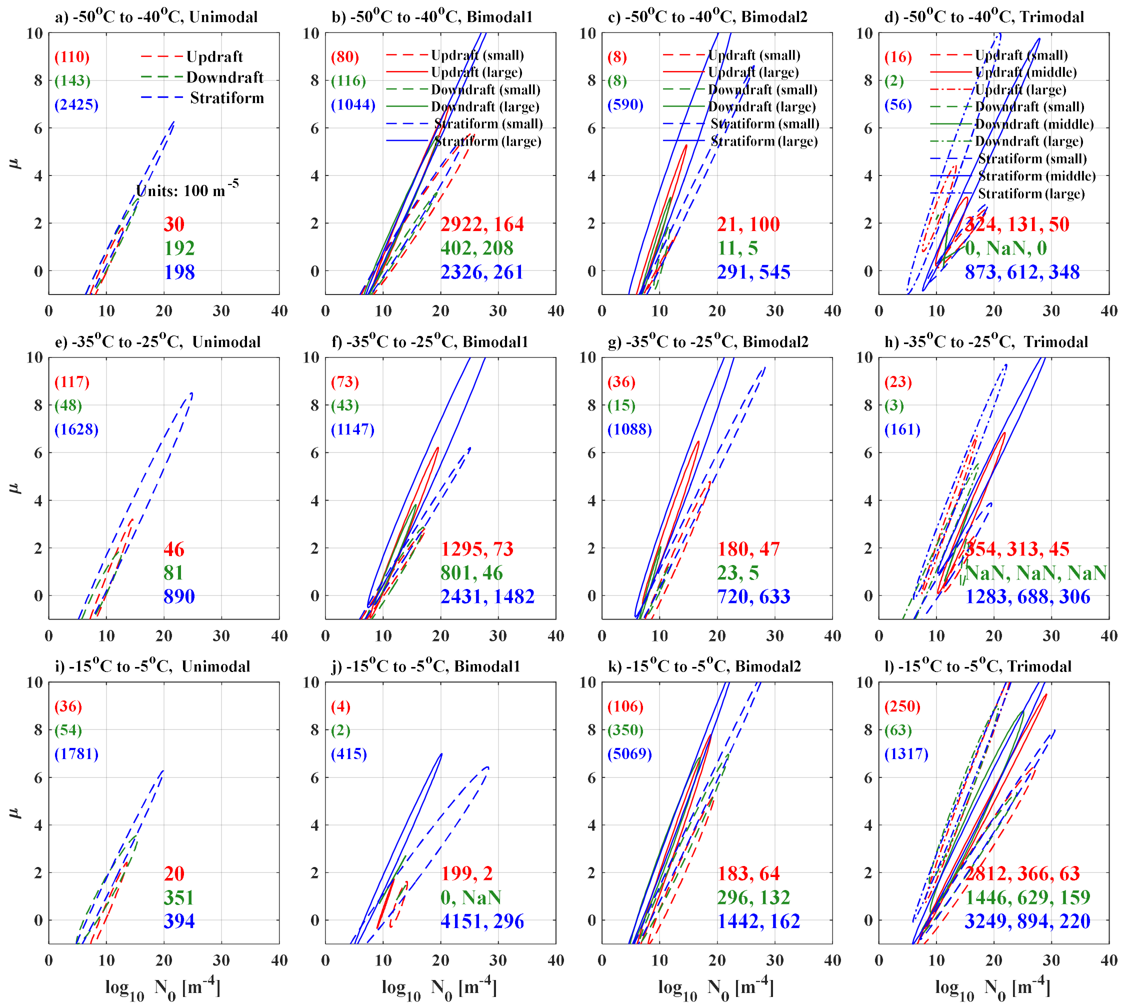

Figure 13. As Figure 7 but segregated according to whether observations obtained in updrafts, downdrafts or stratiform regions. Different line types represent projections of parameters for different modes in *PSDs*. Numbers in brackets give number of sample data points. The volumes of ellipsoid are denoted by colorful numbers and shown in bottom right corner of each subplot. Unimodal *PSDs* have one row, Bimodal *PSDs* have two rows and three rows for Trimodal *PSDs*. The number of columns from left to right represents the mode from small to large. For each column, top row represents updrafts, middle row downdrafts, and bottom row stratiform regions.

updraft (downdraft) was defined as any 5-second period when $w > 1$ m s^{-1} (< -1 m s^{-1}) was sustained for at least four consecutive seconds (Jorgensen et al., 1985; McFarquhar and Black, 2004; Murphy et al., 2017). A stratiform region (i.e., -1 m s$^{-1} \leq w \leq 1$ m s^{-1}) was a period that had neither an updraft nor a downdraft present. Figure 11 shows the normalized frequency of the different modalities for the different vertical motion categories. An apparent feature is that the frequency of Unimodal *PSDs* at −50 °C ≤ T ≤ −40 °C is larger than those at T ≤ −35 °C regardless of vertical motion. Further, the frequency of Bimodal2

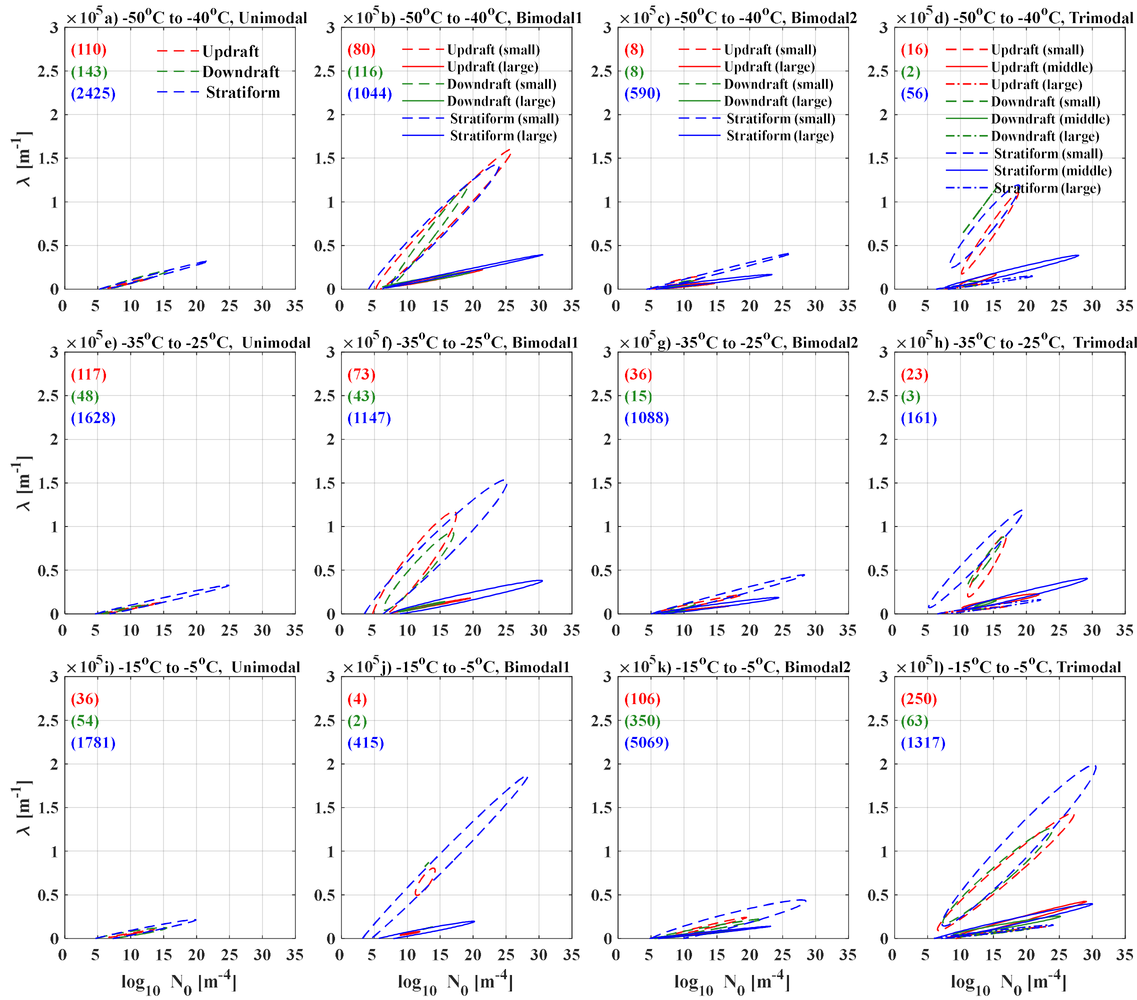

Figure 14. As Figure 8 but segregated according to whether observations obtained in updrafts, downdrafts or stratiform regions.

PSDs and Trimodal *PSDs* both increase as T increases, while the frequency of Bimodal1 *PSDs* decreases with increasing T regardless of vertical motion. Despite trends with T dominating any trend with vertical motion, there is still a clear trend in that the frequency of Trimodal *PSDs* in updrafts is more frequent than for downdrafts or stratiform regions, especially for −15 °C ≤ T ≤ −5 °C (Fig. 11c). This is consistent with previously noted trends in *IWC* (Fig. 5) because the *IWCs* in updrafts are larger than those in the other areas. The frequency of Bimodal *PSDs* is the largest (~ 75%) in downdrafts −15 °C ≤ T ≤ −5 °C (Fig. 11c).

Figure 12 shows the mean (solid line) and median (dashed line) *PSDs* for different vertical velocities as a function of T for all modality *PSDs*. Consistent with trends in Fig.

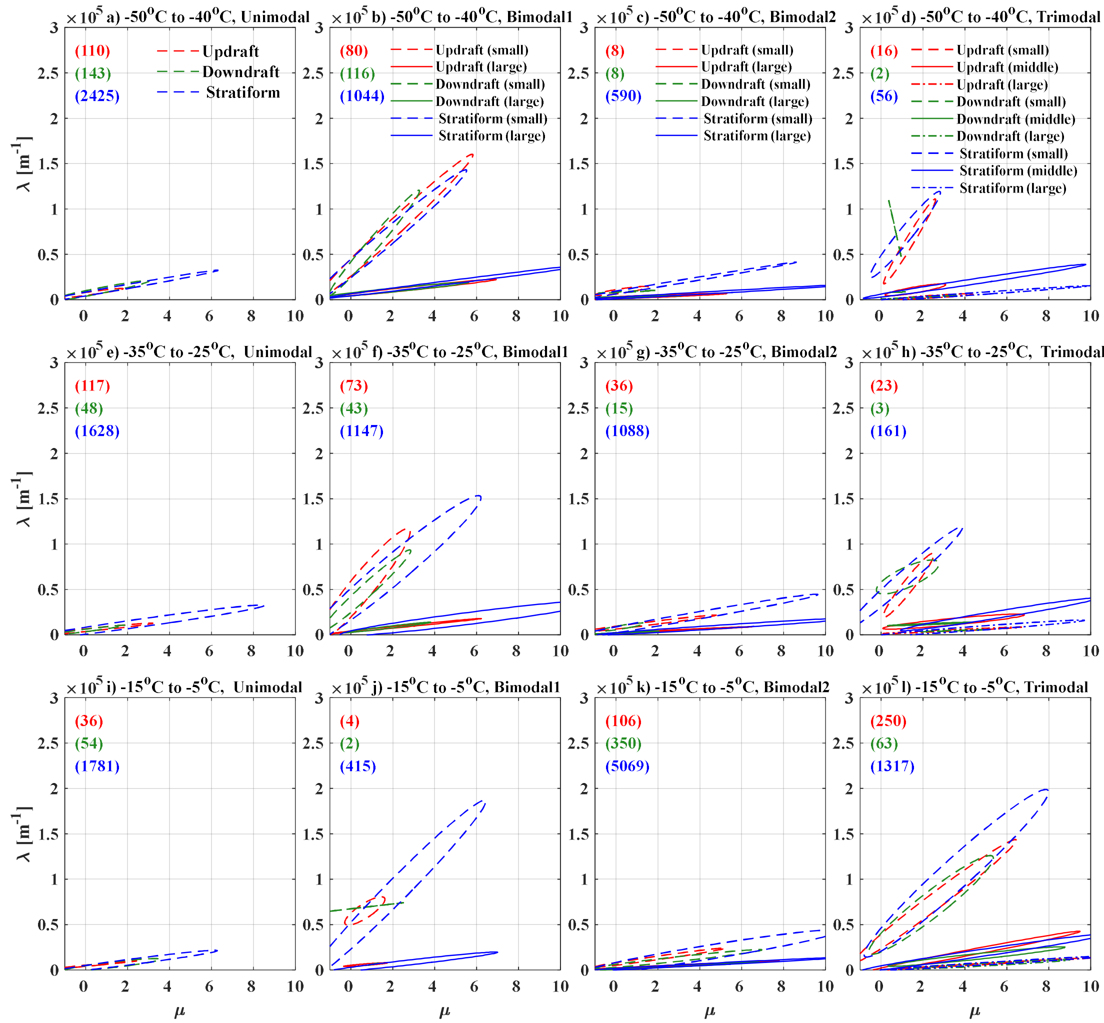

Figure 15. As Figure 9 but segregated according to whether observations obtained in updrafts, downdrafts or stratiform regions.

11, the *PSDs* are more dependent on T than on vertical motion. But there is some dependence on vertical motion. There are typically more small ice crystals (< 500 μm) in updrafts than in other regions for the same modality and T, similar to the finding of Mascio et al. (2020) showing that *N(D)* is smallest for stratiform regions, consistent with updrafts regions being the source region of small ice crystals. The mean breakpoints between the two modes for Bimodal1 *PSDs* are on the average of 100 ± 30 μm with no obvious dependence on *T*. The mean breakpoints between the two modes for Bimodal2 *PSDs* are in the range of 992 to 1168 μm when −15 °C ≤ *T* ≤ −5 °C, but decrease with decreasing *T*, becoming less than 950 μm for −50 °C ≤ *T* ≤ −40 °C. There is no obvious dependence of the breakpoints on vertical velocity. For the Trimodal *PSDs*, the mean breakpoints between

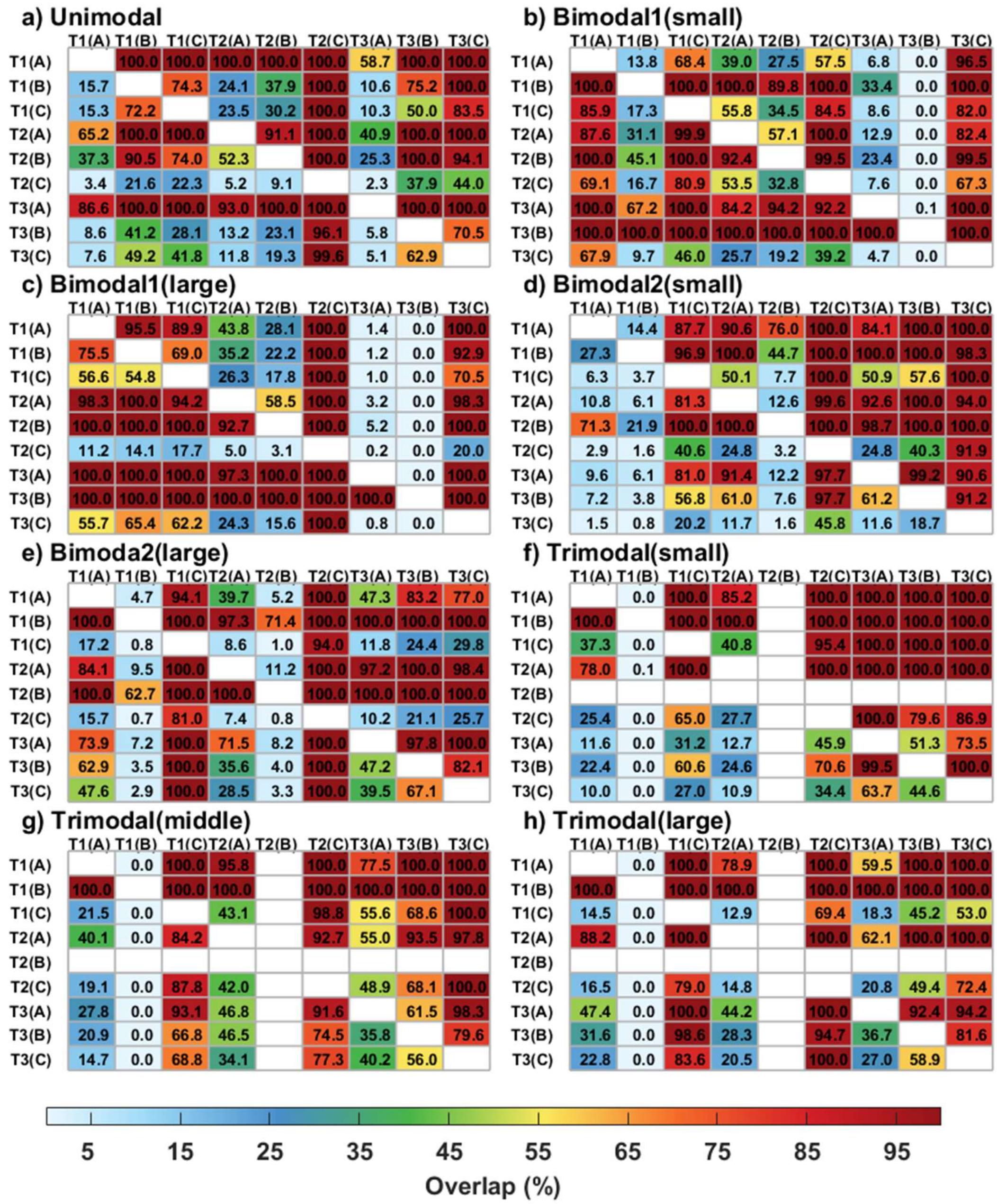

Figure 16. As Figure 10 but for different vertical velocities. A, B and C represents three cloud types: updrafts, downdrafts and stratiform regions respectively. *T1*, *T2* and *T3* represent −50 °C ≤ *T* ≤ −40 °C, −35 °C ≤ *T* ≤ −25 °C and −15 °C ≤ *T* ≤ −5 °C respectively.

the small mode and middle mode are in the range of 85 to 128 μm, and the mean breakpoints between the middle mode and large mode are in the range of 850 to 1200 μm, with no strong dependence on either *T* or vertical motion. The small breakpoints and large breakpoints in Trimodal *PSDs* are similar to the breakpoints in Bimodal1 *PSDs* and in Bimodal2 *PSDs* respectively, with the same trends for the varying vertical motion.

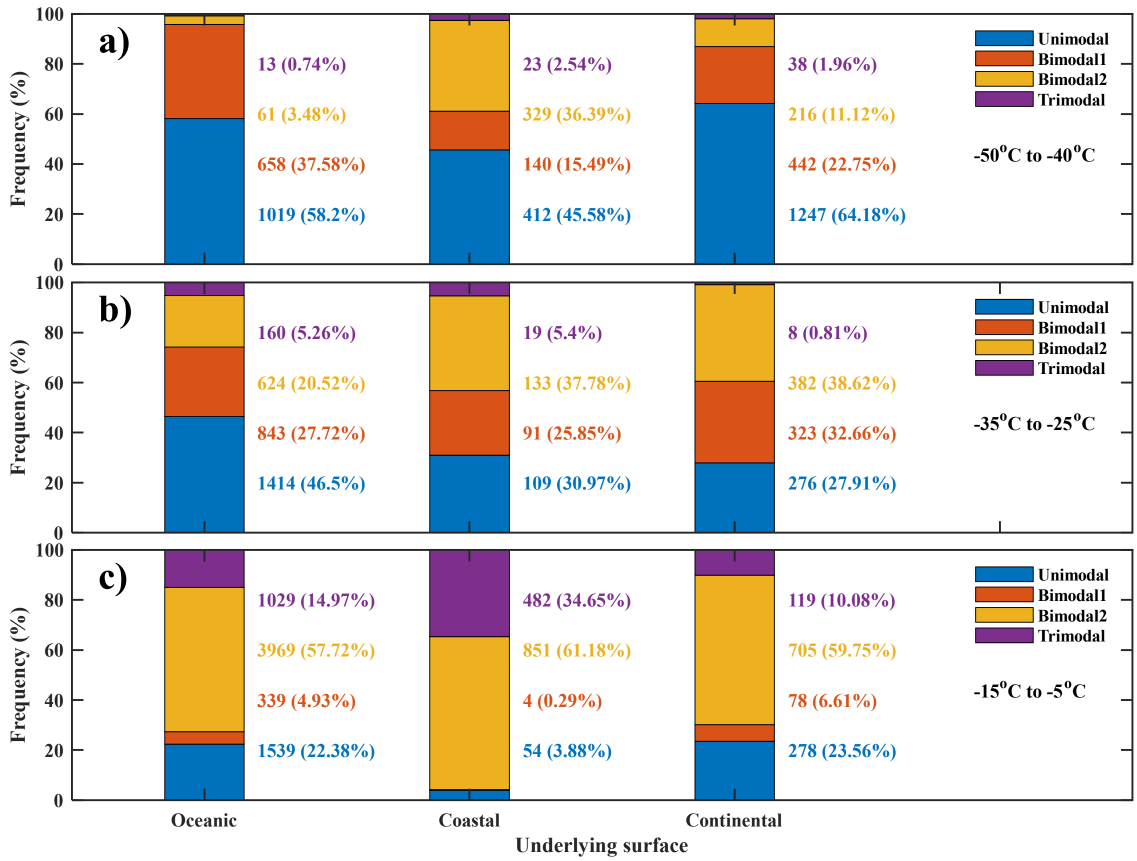

Figure 17. As Figure 5 but segregated according to whether observations obtained in MCSs over different underlying surface characteristics (land, ocean, or coastal line).

Figure 13 shows the ellipse projections of the fit parameters in (N_o, μ) phase space for different modalities and vertical velocities as a function of *T*. The slopes of N_o with λ in the small mode of the Trimodal *PSDs* are largest, and in the large mode of the Trimodal *PSDs* are smallest. There are less obvious changes of the slopes as *T* changes. However, the ellipses of stratiform regions are larger than those for updrafts and downdrafts. N_o and μ can reach larger values in stratiform regions compared to values within updrafts and downdrafts because the *IWC* is smaller in stratiform regions than in updrafts and downdrafts (Hu et al., 2021).

Figure 14 shows the ellipse projections of the fit parameters in (N_o, λ) phase space for different modalities and vertical velocities as a function of *T*. For all modalities, λ increases with increasing N_o. Although there is no strong difference in the slopes of N_o and λ on modality for the same *T*, the ellipses describing stratiform regions tend to be larger than those associated with other vertical motions. The N_o and λ have smaller values in updrafts, consistent with the more likely occurrence of HIWC regions in updrafts and the smaller ellipsoid volumes for the HIWC regions. However, Mascio et al. (2020) found N_o and λ are the largest for updrafts. This difference probably occurs because data were sampled under different meteorological conditions.

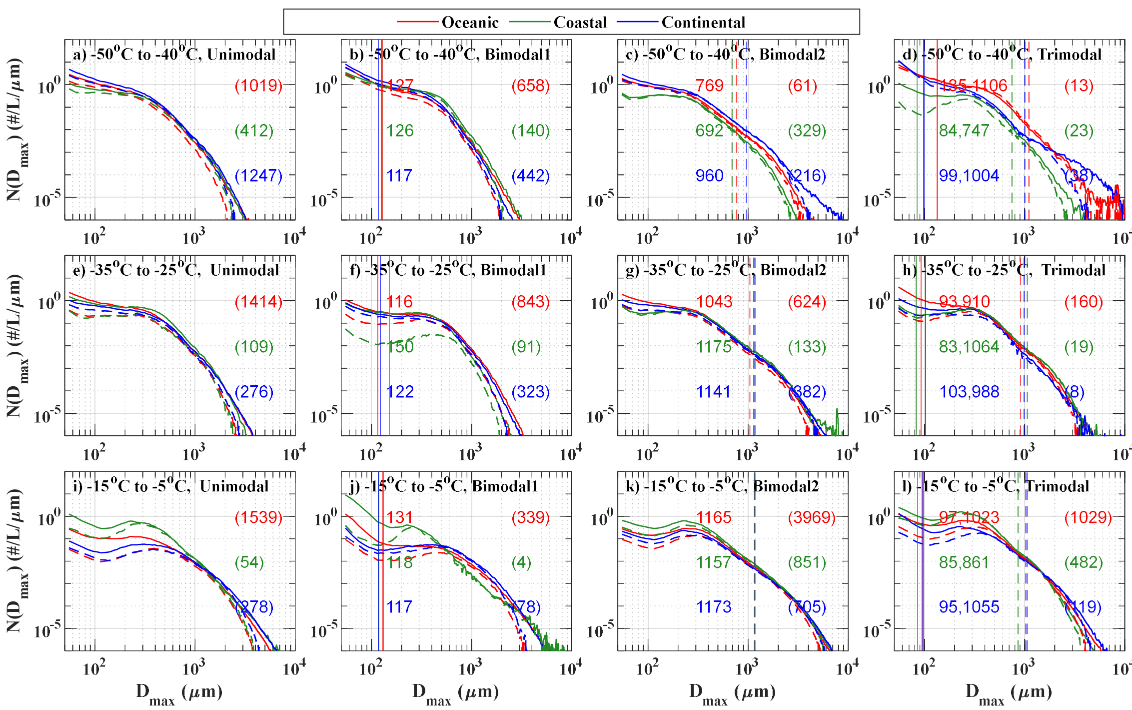

Figure 18. As Figure 6 but segregated according to whether observations obtained in MCSs over different underlying surface characteristics (land, ocean, or coastal line).

Figure15 shows the projections of fit parameters in (μ, λ) phase space. Similar to the (N_o, λ) and (N_o, μ) phase spaces, the slopes of the long axis of the ellipse in (μ, λ) phase space are positive regardless of modality or *T*. The ellipses of stratiform regions are usually larger than those for updraft and downdraft regions for most situations. For Trimodal *PSDs*, there are obvious difference of slopes between the small mode and middle mode, and less obvious difference between middle mode and large mode.

To quantify how the fit parameters vary with vertical motion, Figure 16 shows the overlap fraction between the ellipsoid volumes for different T and vertical motions. For the same T, volumes in stratiform regions are usually larger for updrafts and downdrafts regardless of modality. For example, the percent overlap is usually less than 70% for stratiform regions when $-15\ ^\circ\mathrm{C} \le T \le -5\ ^\circ\mathrm{C}$. Further, the volumes in downdrafts are usually larger than for updrafts regions.

c. Surface characteristics

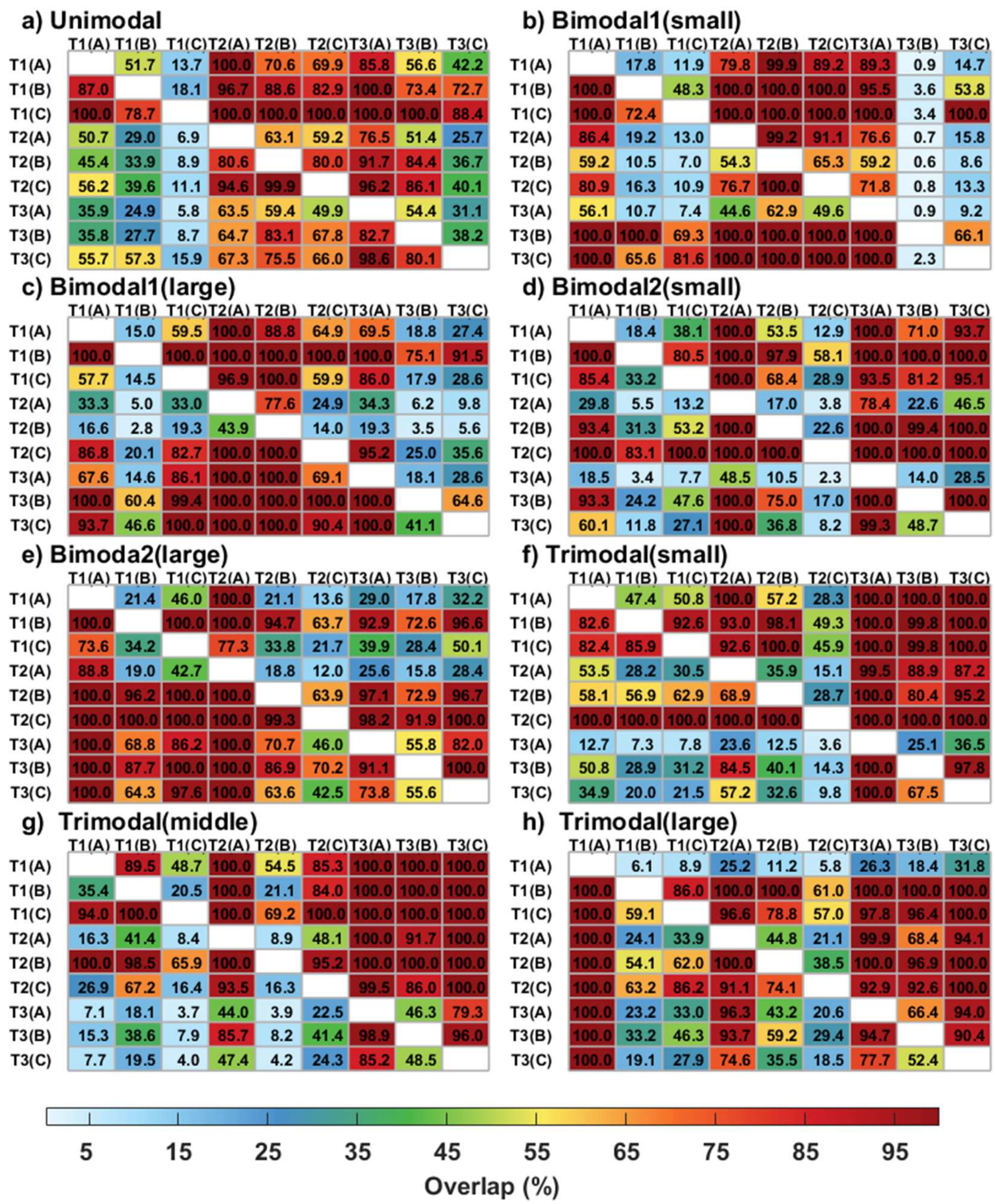

Figure 19. As Figure 10 but for different underlying surface characteristics. A, B and C represents underlying surface characteristics: oceanic, coastal and continental MCSs respectively. *T1*, *T2* and *T3* represent −50 °C ≤ *T* ≤ −40 °C, −35 °C ≤ *T* ≤ −25 °C and −15 °C ≤ *T* ≤ −5 °C respectively.

The MCSs were separated into three groups according to whether the convection was observed over the ocean, coastline, or land to compare *PSDs* as a function of surface characteristics. Figure 17 shows the normalized frequency of the different modalities of these regions as a function of *T*. The dependence on *T* seems to be stronger than any dependence on surface characteristics. For example, the frequency of Unimodal *PSDs* increases and the frequency of multimodal *PSDs* decreases with decreasing *T* regardless of surface type. The frequency of multimodal *PSDs* in coastal MCSs is usually larger than for oceanic or continental convection at the same *T*, especially for −15 °C ≤ *T* ≤ −5 °C when multimodal *PSDs* occur ~ 96.1% of the time (Fig. 17c). Among the multimodal *PSDs*, the frequency of Bimodal2 *PSDs* in coastal MCSs is usually largest reaching ~ 61.5% of the time when −15 °C ≤ *T* ≤ −5 °C (Fig. 17c). The frequency of Trimodal *PSDs* for continental MCSs are smaller than those for oceanic MCSs when *T* ≤ −35 °C, but an opposite trend is noted when −50 °C ≤ *T* ≤ −40 °C. This is consistent with the findings that higher *IWCs* are found in oceanic MCSs at lower altitude and higher *IWCs* in continental MCSs at higher altitude (Hu et al., 2021).

Figure 18 shows the mean (solid line) and median (dashed line) *PSDs* for different surface characteristics as a function of *T*. The number of small ice crystals with D_{max} < 100 μm in continental MCSs is smaller than for the other surface characteristics when −15 °C ≤ *T* ≤ −5 °C, but larger when −50 °C ≤ *T* ≤ −40 °C, because MCSs over the mainland are usually stronger than over the ocean or coast (e.g., Lucas et al., 1994; Zipser et al., 2006; Matsui et al., 2016), and thus produce more small ice crystals. The mean breakpoints between the two modes for Bimodal1 *PSDs* are larger than 100 μm, reaching a maximum of 150 μm for Bimodal1 *PSDs* in Coastal MCSs at −35 °C ≤ *T* ≤ −25 °C. The average breakpoint is 692 μm for Bimodal2 *PSDs* in Coastal MCSs at −50 °C ≤ *T* ≤ −40 °C, smaller than values noted for other *T* and surface characteristics. The mean small breakpoints (83 to 85 μm) and large breakpoints (747 to 1064 μm) for coastal MCS are usually smaller than those in oceanic MCS (93 to 135 μm and 910 to 1106 μm) and continental MCS (95 to 103 μm and 988 to 1055 μm).

To quantify how the ellipsoids describing the fit parameters vary with surface characteristics, Figure 19 shows the overlap between the three-dimensional volumes of equally realizable fit parameters for different surface characteristics. Ellipsoids describing continental MCSs have the smallest volumes for Unimodal *PSDs* at different T, consistent with the parameter ranges being smaller (Figure not shown). The ellipsoid volume overlaps in coastal MCSs at -50 °C $\leq T \leq -40$ °C have the smallest values, and the ellipsoid volume overlaps in oceanic MCSs regions at -15 °C $\leq T \leq -5$ °C have the smallest values for

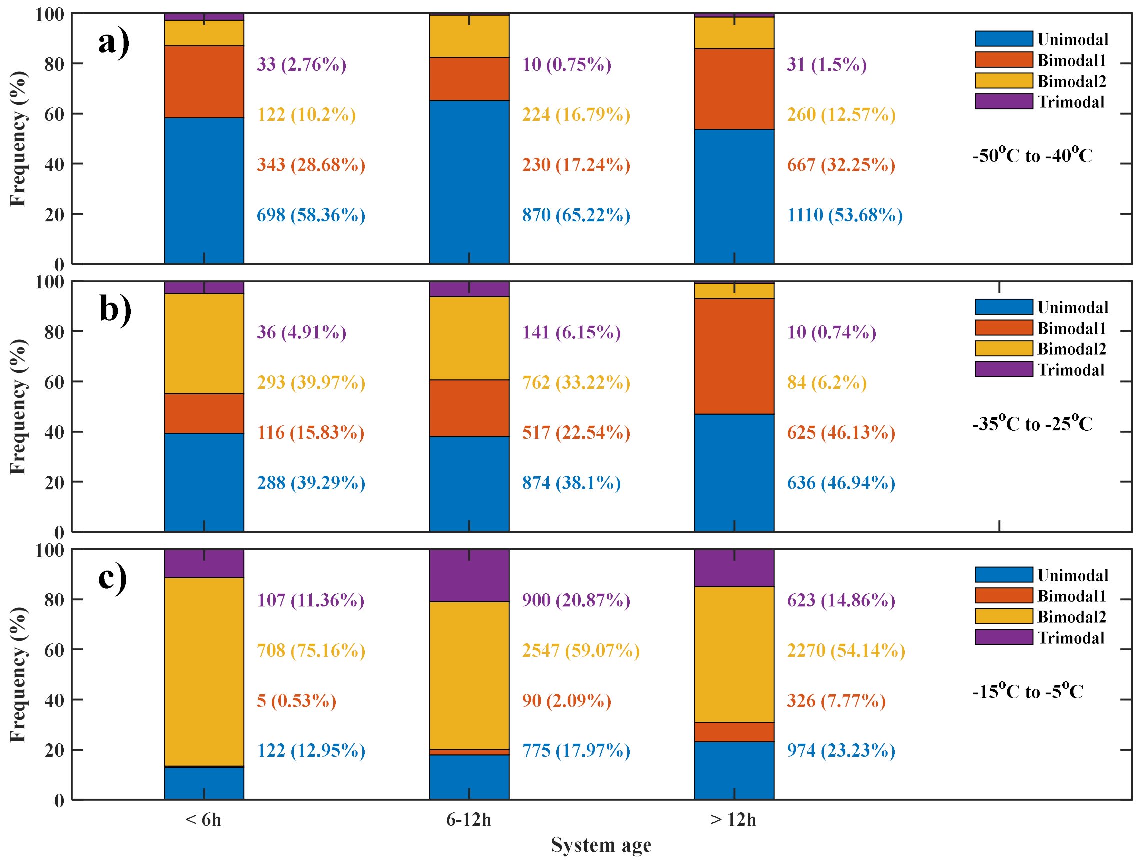

Figure 20. As Figure 5 but segregated according to age of MCS where observations obtained.

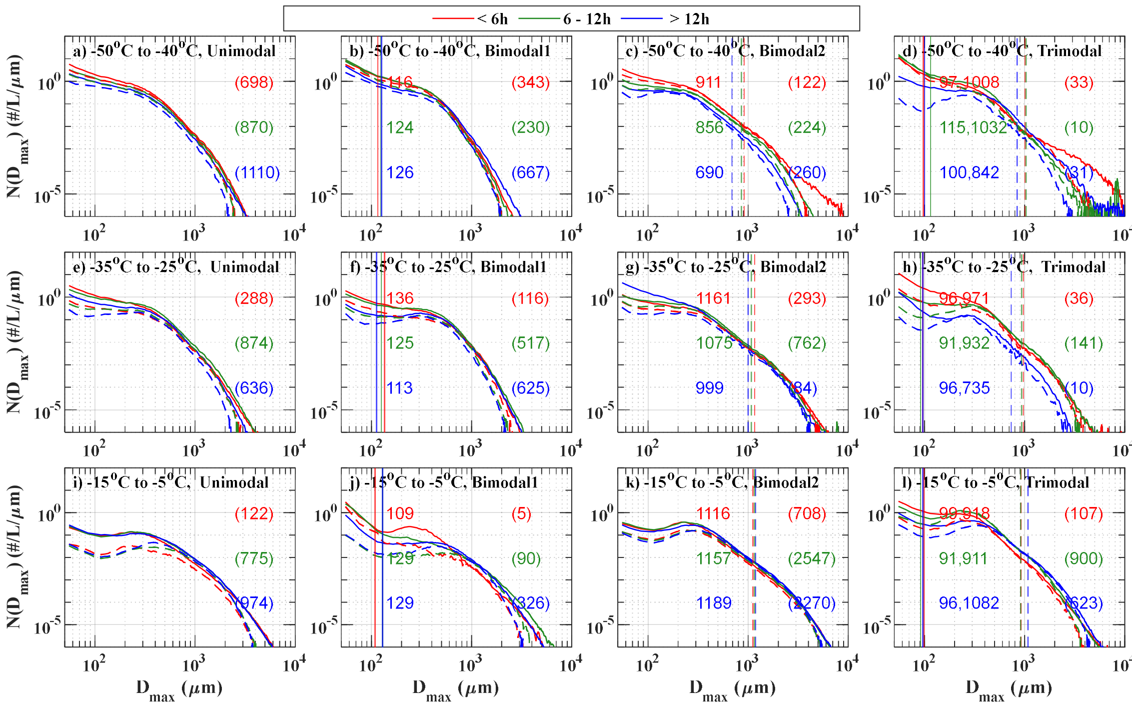

Figure 21. As Figure 6 but segregated according to age of system where observations obtained.

most conditions. And the ellipsoids for coastal MCSs are usually smaller than for oceanic MCSs for different modality *PSDs*.

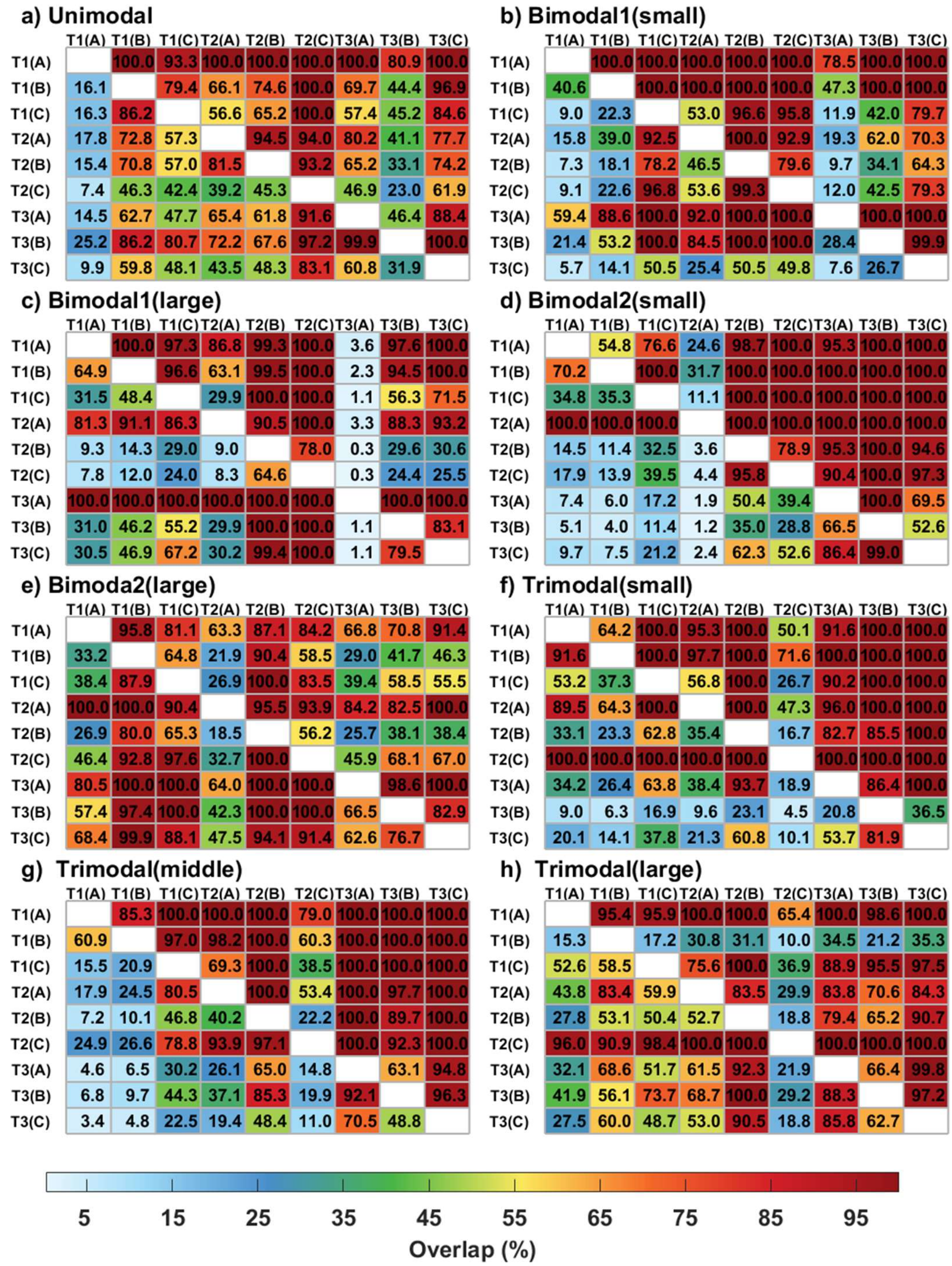

Figure 22. As Figure 10 but segregated according to MCS age. A, B and C represents MCS ages within < 6 h, 6–12 h, and > 12 h respectively. *T1*, *T2* and *T3* represent −50 °C ≤ *T* ≤ −40 °C, −35 °C ≤ *T* ≤ −25 °C and −15 °C ≤ *T* ≤ −5 °C respectively.

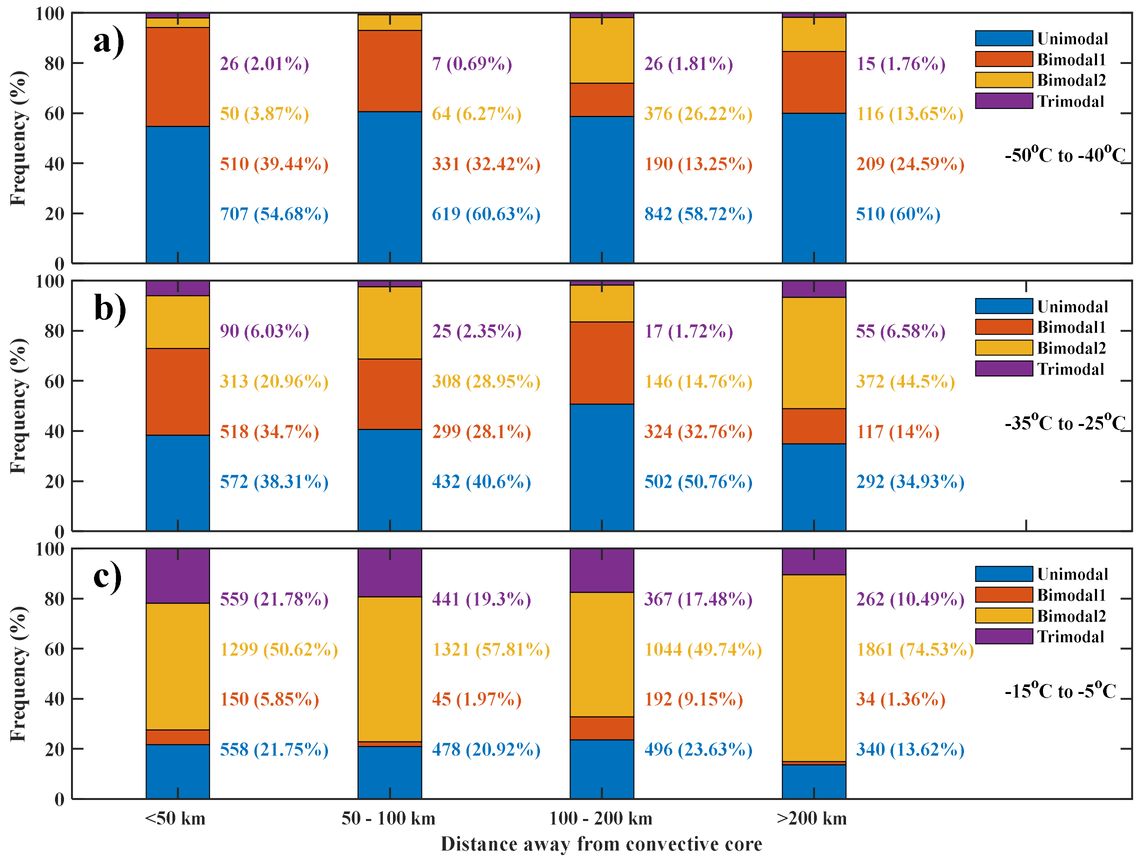

Figure 23. As Figure 5 but segregated according to distance away from convective core where observations obtained.

d. System age

To compare *PSDs* for different system ages, the MCS age was sorted into three groups (< 6 h, 6–12 h, > 12 h). Figure 20 shows the normalized frequency of the different modalities for MCSs with different ages as a function of *T*. There is a stronger dependence of the modality with *T* than on the system age. Nevertheless, the frequency of Unimodal *PSDs* increases with system age for $T \geq -35$ °C, while the frequency of Trimodal *PSDs* is the largest for system age between 6–12 h (Figs. 20b and 20c). This is consistent with the 6–12 h stage representing the developing or mature stage after ice has started being injected into the anvil (Leary and Houze, 1980), with many ice crystals being created and growing by aggregation (Hu et al., 2021). For the multimodal *PSDs*, the frequency of Bimodal1 *PSDs* in MCSs age > 12 h is largest for each *T*, reaching to ~ 46.1% when -35 °C $\leq T \leq$ -25 °C (Fig. 20b). On the other hand, the frequency of Trimodal *PSDs* in MCS ages > 12 h is usually the smallest for $T \leq -25$ °C, due to the *IWC* in the > 12 h age is the smallest, consistent with sublimation and a weakening and dissipation of MCSs not being conducive to the generation and growth of ice particles (Hu et al., 2021).

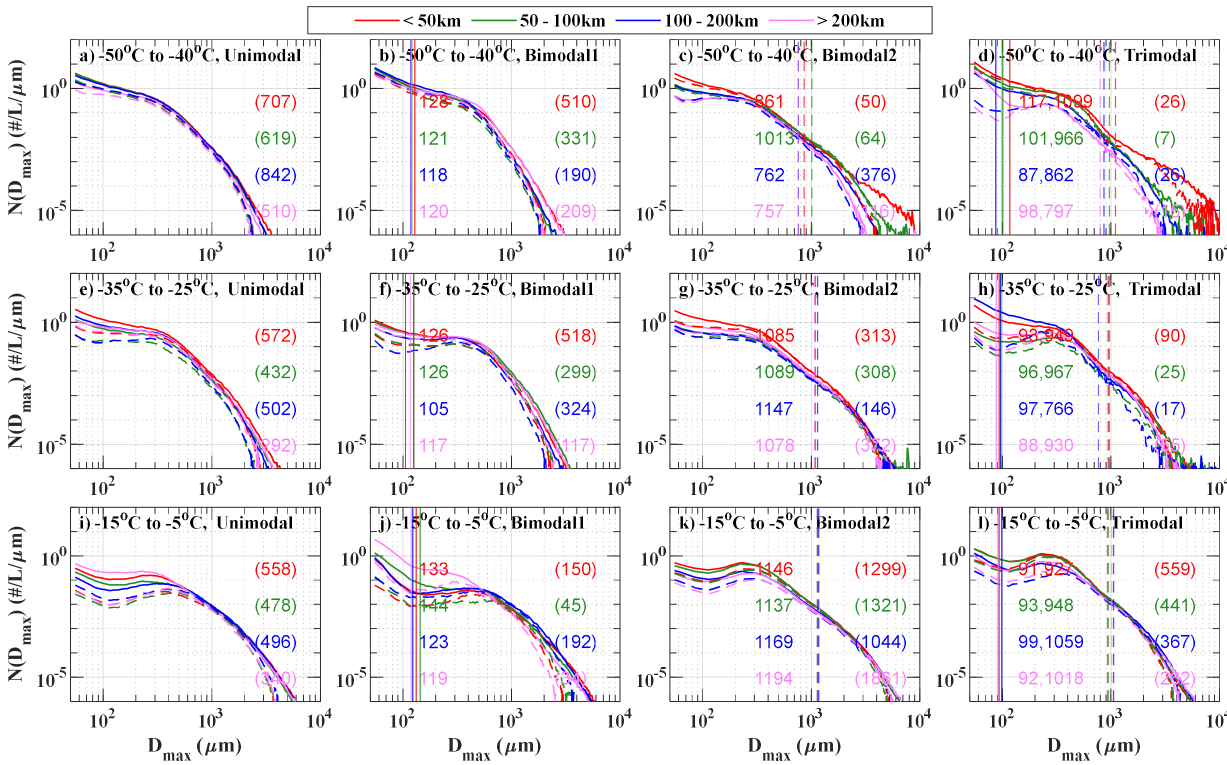

Figure 24. As Figure 6 but segregated according to distance away from convective core where observations obtained.

Figure 21 shows the mean (solid line) and median (dashed line) *PSDs* as a function of MCS age and *T*. For most conditions, the $N(D_{max})$ for younger system ages are usually larger than those in older MCSs for D_{max} < 200 because more ice crystals are produced in the developing and mature stages. The differences between Trimodal *PSDs* for different MCS ages are more obvious than for other modality *PSDs* at all *T*. Breakpoints between the two modes in Bimodal2 *PSDs* increase with increasing *T* for all MCS ages. The breakpoints in Bimodal2 and the breakpoints between the second and third mode in Trimodal *PSDs* are the smallest for MCS ages > 12 h when $T \leq -25$ °C.

To quantify the difference between the overlapping ellipsoids of equally plausible solutions for different *T* and MCS ages, Figure 22 shows the overlap between the three-dimensional volumes of equally realizable fit parameters for different MCS ages and *T* for the four modalities. The most apparent feature is that for different modality *PSDs*, the ellipsoid volumes for MCSs with ages < 6 h at -50 °C $\leq T \leq -40$ °C are largest. For example, for the small mode of Bimodal2 *PSDs*, the overlaps are mostly less than 80% when MCS ages are in < 6 h at −50 °C ≤ *T* ≤ −40 °C , while more than 80% are found in other ellipsoids (Fig. 22d).

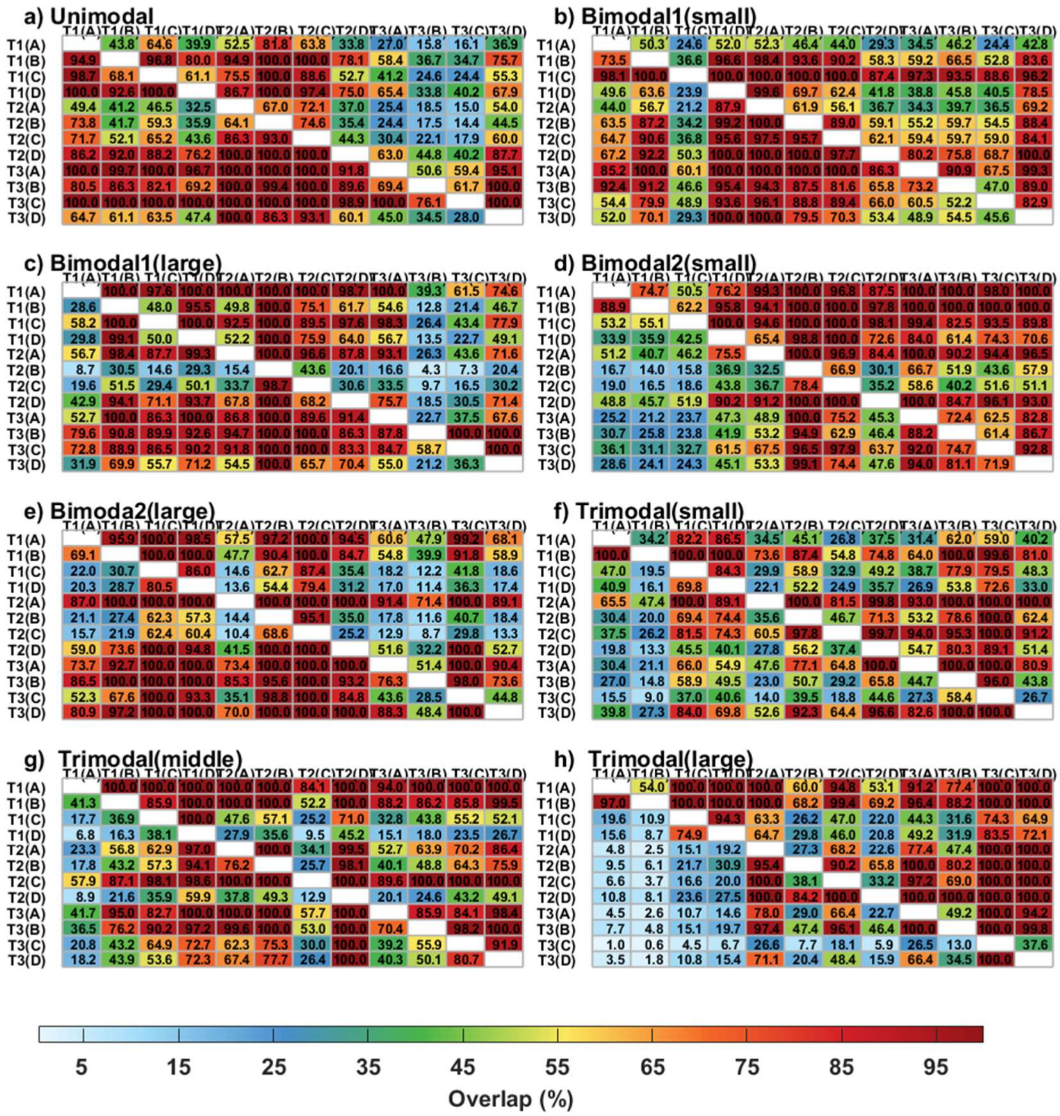

Figure 25. As Figure 10 but segregated according to distance away from convective core where observations obtained. A, B, C and D represent four regions within *L* ≤ 50 km, 50 km < *L* ≤ 100 km, 100 km < *L* ≤ 200 km, *L* > 200 km respectively. *T1*, *T2* and *T3* represent −50 °C ≤ *T* ≤ −40 °C, −35 °C ≤ *T* ≤ −25 °C and −15 °C ≤ *T* ≤ −5 °C respectively.

e. Distance away from the convective core

In order to compare the *PSDs* with distance away from the convective core (*L*), *PSDs* were divided into four groups (*L* ≤ 50 km, 50 km < *L* ≤ 100 km, 100 km < *L* ≤ 200 km, *L* > 200 km). Figure 23 shows the normalized frequency of the four different modalities as a function of L and T. The dependence on T is stronger than the dependence on L. However, there are still some trends with L. The frequency of Trimodal *PSDs* decreases slowly with increasing L when -15 °C $\leq T \leq -5$ °C, and the frequency of Bimodal2 *PSDs* is larger for regions away from the convective core when $T \leq -25$ °C, while the opposite trends are realized for Bimodal1 *PSDs* (Fig. 23a and 23b) as the frequency of Bimodal1 *PSDs* is smallest for these regions at the same T. In summary, changes in the frequency of *PSD* modality with L is less obvious, probably due to horizontal wind transport. T is still the important factor, the frequency of Unimodal *PSDs* increases, and multimodal *PSDs* decrease with decreasing T for different L.

Figure 24 shows the mean (solid line) and median (dashed line) *PSDs* as a function of T and L. There are less obvious differences for Unimodal, Bimodal1 and Bimodal2 *PSDs* between different L at the same T. Breakpoints between the two modes in Bimodal1 *PSDs* show less obvious changes with increasing T, the breakpoints between the two modes in Bimodal2 *PSDs* within different L increase with increasing T. For example, the mean breakpoint is 757 µm for Bimodal2 *PSDs* with $L > 200$ km when -50 °C $\leq T \leq -40$ °C, while it increases to 1194 µm when -15 °C $\leq T \leq -5$ °C. Less obvious difference between the breakpoints within different L for the same modality *PSDs* and same T.

To quantify the difference between the ellipsoids of equally plausible solutions for different L, Figure 25 shows the overlap between the three-dimensional volumes of equally realizable fit parameters for different L and T for the four modalities. Less obvious regular trends between different L at the same T, consistent with the finding of Mascio et al. (2020), due to the distributions of *IWCs* with L are different at different T (Korolev et al., 2018; Hu et al., 2021).

5. Conclusions

To quantitatively describe the difference of particle size distributions (*PSDs*) as a function of environmental conditions, data obtained during the second HAIC-HIWC flight campaign conducted from 9–29 May 2015 out of Cayenne, French Guiana were analyzed. Data were separated according to temperature (T, -15 °C $\leq T \leq -5$ °C; -35 °C $\leq T \leq -25$ °C; -50 °C $\leq T \leq -40$ °C), vertical velocity (updrafts, downdrafts, and stratiform cloud regions), surface conditions (oceanic, coastal and continental), MCS age (< 6 h, 6–12h, > 12 h), and distance away from the convective core ($L \leq 50$ km, 50 km $< L \leq 100$ km, 100 km < $L \leq 200$ km, $L > 200$ km). The difference of *PSDs* between HIWC regions was also contrasted against those obtained in regions without HIWCs. The principal findings of this study are as follows:

1. HIWC regions ($IWC \geq 1.5$ g m^{-3}) with small *MMD* (< 500 μm) are full of small columns and irregular ice crystals at -15 °C $\leq T \leq -5$ °C, consistent with negative correlation between *IWC* and *MMD* within the HIWC regions. The distributions of ice crystals shapes are different for different *IWC* regions.
2. Data from the Cayenne campaign were used to determine how many modes were required to represent the *PSD* using a new methodology that automatically determines the number of modes and gamma fit parameters for each mode in a multimodal *PSD*. Four kinds of modalities of *PSDs* were found by this method.
3. The *T* has the largest effect on *PSD* shape, and hence on the number of modes and the fit parameters describing each mode of the *PSDs*. The frequency of multimodal *PSDs* increases and the frequency of unimodal *PSD* decreases with increasing *T*, consistent with heterogeneous nucleation in the presence of particles sedimenting from above (Zhao et al., 2010) and the aggregation process.
4. The number and location of the modes in a *PSD* (modalities) are also related to *IWC*. The frequency of multimodal *PSDs* increases with *IWC* and the frequency of unimodal *PSDs* decreases with *IWC*. There was no strong trend in how frequency distributions of *IWC* and *MMD* varied with the modality of the *PSD*.
5. The frequency of Unimodal and multimodal *PSDs* depends on vertical velocity (*w*), consistent with the impact of *w* on *IWC*. The largest frequency of Trimodal *PSDs* occurs in updrafts. There is some dependence on the distributions of modality on other environmental conditions (e.g., underlying surface characteristics, MCS age, the distance away from the convective core), which is not as strong as the dependence on *T* and can be related to the dependence of *IWC* on environmental conditions.

6. The breakpoints between the two modes in the Bimodal1 *PSDs* occur at a D_{max} of 100 ± 20 μm with no strong dependence on *T*. Breakpoints between the two modes in the Bimodal2 *PSDs* are located at a D_{max} of around 1000 ± 300 μm and increase with *T*. The breakpoints that exist in Trimodal *PSDs* are similar to the breakpoints in the two types of bimodal *PSDs*.
7. The three fit parameters (N_o-λ-μ) characterizing the gamma distribution of each mode are interdependent. For the same λ, N_o and μ are larger in the large modes with larger D_{max} compared to the small modes, consistent with particles with smaller D_{max} consisting of recently nucleated particles that have not significantly grown by vapor deposition, and particles with larger D_{max} having undergone sorting by sedimentation and deposition (Jackson et al., 2015).
8. The μ decreases with *IWC* for the same N_o, and the ranges of λ and N_o both narrow with increasing *IWC*. This consistent with more smaller ice crystals being found in the high *IWC* regions.
9. The HIWC regions have the smallest ellipsoids, indicating that the parameters (N_o, μ, and λ) are constrained for HIWC regions compared to other regions and also meaning the least uncertainty in parameters for such conditions.

The findings presented here apply only to data collected in the vicinity of Cayenne, French Guiana during HAIC-HIWC. The techniques developed here can be applied to data collected elsewhere to determine the robustness of the findings. Future studies should seek to obtain data on more diverse geographic locations, and implement parameterizations of *PSDs* developed here in ensemble or stochastic simulations that can be used to test processes responsible to occurrence of large numbers of small ice crystals. Model simulations using parameterizations of *PSDs* with three modes should be conducted to see if they improve upon simulations conducted using one-mode parameterizations as such simulations should better represent processes without the additional computational expense of a bin-resolved scheme. Future work also needs to better determine reasons for the variability of surfaces characterizing the *PSDs*, including examining whether the surfaces and the modality vary with concentrations of cloud condensation nuclei and ice nucleating particles. In addition, care should be taken to isolate the differences in the *PSD* surfaces that are caused by variations in meteorological and aerosol conditions, as opposed to differences that arise due to differences in probes used to collect the data and algorithms used to process the data.

Data Availability Statement.

Observation data are available at https://data. eol.ucar.edu/master_lists/generated/haic-hiwc_2015. The GOES-13 data are available over the domain of (0-10ºN, 45-60ºW) where the aircraft flew during the Cayenne campaign (https://doi.org/10.5065/D6NC5ZX6).

Acknowledgments.

This work was supported by the National Science Foundation (Award Numbers: 1213311 and 1842094). Observation data are provided through NCAR/EOL under the sponsorship of the National Science Foundation (https://data.eol.ucar.edu/). NCAR is sponsored by the National Science Foundation. Major North American funding for flight campaigns was provided by the FAA William Hughes Technical Center and Aviation Weather Research Program, the NASA Aeronautics Research Mission Directorate Aviation Safety Program, the Boeing Co., Environment and Climate Change Canada, the National Research Council of Canada, and Transport Canada. Major European campaign and research funding was provided from (i) the European Commission Seventh Framework Program in research, technological development and demonstration under grant agreement ACP2-GA-2012-314314, (ii) the European Safety Agency (EASA) Research Program under service contract EASA.2013.FC27. Further funding was provided by the Ice Crystal Consortium. Some of the computing for this project was performed at the University of Oklahoma (OU) Supercomputing Center for Education and Research (OSCER). The discussions of HIWC conditions and aircraft measurements with Walter Strapp are greatly appreciated. The first author is also supported by the China Scholarship Council (CSC). The authors are also grateful to all of whom provided helpful comments and suggestions that improved the manuscript.

References

Ackerman, T. P., K. N. Liou, F. P. Valero, and L. Pfister, 1988: Heating rates in tropical anvils. *J. Atmos. Sci.,* **45,** 1606–1623, doi:10.1175/1520-0469(1988)045,1606: HRITA.2.0.CO;2.

Bailey, M. P., and Hallett, J., 2009: A comprehensive habit diagram for atmospheric ice crystals: Confirmation from the laboratory, AIRS II, and other field studies. *J. Atmos. Sci.,* **66,** 2888–2899. https://doi.org/10.1175/2009JAS2883.1

Baumgardner, D., Abel, S. J., Axisa, D., Cotton, R., Crosier, J., Field, P., Gurganus, C., Heymsfield, A., Korolev, A., Krämer, M., Lawson, P., McFarquhar, G., Ulanowski, Z., and Um, J., 2017: Cloud Ice Properties: In Situ Measurement Challenges. *Meteor. Monogr.,* **58,** 9.1-9.23, available from: https://doi.org/10.1175/AMSMONOGRAPHS-D-16-0011.1

Brechner, P., 2021: Ice Crystal Size Distributions in Tropical Mesoscale Convective Systems in the Vicinity of Darwin, Australia: Results from the HAIC/HIWC Campaign. M.S. thesis, School of Meteorology, University of Oklahoma, 57 pp. [Available online at https://hdl.handle.net/11244/332327.]

Brown, P. R., and P. N. Francis, 1995: Improved measurements of the ice water content in cirrus using a total-water probe. *J. Atmos. Oceanic Technol.*, **12,** 410–414, doi:10.1175/ 1520-0426(1995)012,0410:IMOTIW.2.0.CO;2.

Bryan, G. H., and H. Morrison, 2012: Sensitivity of a simulated squall line to horizontal resolution and parameterization of microphysics, *Mon. Weather Rev.,* **140,** 202–225, doi:10.1175/MWR-D-11-00046.1.

Chandrasekar, V., and V. N. Bringi, 1987: Simulation of radar reflectivity and surface measurements of rainfall. *J. Atmos. Oceanic Technol.,* **4,** 464–478, doi:10.1175/1520-0426(1987)004,0464: SORRAS.2.0.CO;2.

Chen, C. H., Su, C. L., Chen, J. H., and Chu, Y. H., 2020: Vertical Wind Effect on Slope and Shape Parameters of Gamma Drop Size Distribution. *J. Atmos. Oceanic Technol.,* **37,** 243-262.

Chen, S. and Cotton, W., 1988: The sensitivity of a simulated extratropical mesoscale convective system to longwave radiation and ice-phase microphysics, *J. Atmos. Sci.,* **45,** 3897–3910, https://doi.org/10.1175/1520- 0469(1988)045<3897:TSOASE>2.0.CO;2.

Clark, A. J., Weiss, S. J., Kain, J. S., Jirak, I. L., Coniglio, M., Melick, C. J., Siewert, C., Sobash,

R. A., Marsh, P. T., Dean, A. R., Xue, M., Kong, F., Thomas, K. W., Wang, Y., Brewster, K., Gao, J., Wang, X., Du, J., Novak, D. R., Barthold, F. E., Bodner, M. J., Levit, J. J., Entwistle, C. B., Jensen, T. L., and Correia, J., Jr., 2012: An Overview of the 2010 Hazardous Weather Testbed Experimental Forecast Program Spring Experiment. *Bull. Amer. Meteor. Soc.,* **93,** 55-74, https://doi.org/10.1175/BAMS-D-11-00040.1

Del Genio, A. D., and W. Kovari, 2002: Climatic properties of tropical precipitating convection under varying environmental conditions. *J. Climate,* **15,** 2597–2615.

Dezitter, F., A. Grandin, J. L. Brenguier, F. Hervy, H. Schlager, P. Villedieu, and G. Zalamansky, 2013: HAIC (High altitude ice crystals). Proc. Fifth AIAA Atmospheric and Space Environments Conf., San Diego, CA, American Institute of Aeronautics and Astronautics, AIAA-2013-2674. [Available online at http://arc.aiaa.org/doi/abs/10.2514/6.2013-2674.]

Ding, S., McFarquhar, G. M., Nesbitt, S. W., Chase, R. J., Poellot, M. R., and Wang, H., 2020: Dependence of mass–dimensional relationships on median mass diameter. *Atmos.*, **11,** 756.

DMT, 2009: Single particle imaging. Data analysis user's guide, DOC-0223, Rev. A, 34 pp.

Finlon, J. A., McFarquhar, G. M., Nesbitt, S. W., Rauber, R. M., Morrison, H., Wu, W., and Zhang, P., 2019: A novel approach for characterizing the variability in mass–dimension relationships: Results from MC3E. *Atmos. Chem. and Phy.*, **19,** 3621-3643.

Fontaine, E., Leroy, D., Schwarzenboeck, A., Delanoë, J., Protat, A., Dezitter, F., Grandin, A., Strapp, J. W., and Lilie, L. E., 2017: Evaluation of radar reflectivity factor simulations of ice crystal populations from in situ observations for the retrieval of condensed water content in tropical mesoscale convective systems, *Atmos. Meas. Tech.,* **10,** 2239–2252, 2017.

Field, P. R., Hogan, R. J., Brown, P. R. A., Illingworth, A. J., Choularton, T. W., and Cotton, R. J., 2005: Parametrization of ice-particle size distributions for mid-latitude stratiform cloud. *Quart. J. Roy. Meteor. Soc.,* **131,** 1997-2017.

Fu, Q., S. K. Krueger, and K. N. Liou, 1995: Interactions of radiation and convection in simulated tropical cloud clusters. *J. Atmos. Sci.,* **52,** 1310–1328.

Fu, Q., 1996: An accurate parameterization of the solar radiative properties of cirrus clouds for climate models, *J. Clim.,* **9,** 2058–2082.

Gilmore, M. S., J. M. Straka, and E. N. Rasmussen, 2004: Precipitation uncertainty due to variations in precipitation parti- cle parameters within a simple microphysics scheme. *Mon. Wea. Rev.,* **132,** 2610–2627, doi:10.1175/MWR2810.1.

Gu, Y., Liou, K. N., Ou, S. C., and Fovell, R., 2011: Cirrus cloud simulations using WRF with improved radiation parameterization and increased vertical resolution, *J. Geophys. Res.,* **116,** D06119, https://doi.org/10.1029/2010JD014574, 2011.

Gunn, K. L. S., and J. S. Marshall, 1958: The distribution with size of aggregate snowflakes. *J. Meteor.,* **15,** 452–461, doi:10.1175/ 1520-0469(1958)015,0452:TDWSOA.2.0.CO;2.

Haddad, Z. S., S. L. Durden, and E. Im, 1996: Parameterizing the raindrop size distribution. J. *Appl. Meteor.,* **35,** 3–13, doi:10.1175/ 1520-0450(1996)035,0003:PTRSD.2.0.CO;2.

Handwerker, J., and Straub, W., 2011: Optimal determination of parameters for gamma-type drop size distributions based on moments. *J. Atmos. Oceanic Technol.,* **28,** 513-529.

Heymsfield, A. J., and G. M. McFarquhar, 2002: Mid-latitude and tropical cirrus microphysical properties. Cirrus, D. K. Lynch, Ed., Oxford University Press, 78–101.

Heymsfield, A. J., Bansemer, A., Heymsfield, G., and Fierro, A. O., 2009: Microphysics of maritime tropical convective updrafts at temperatures from −20° to −60°. *J. Atmos. Sci.,* **66,** 3530–3562, doi:10.1175/2009JAS3107.1.

Heymsfield, A. J., C. Schmitt, and A. Bansemer, 2013: Ice cloud particle size distributions and pressure-dependent terminal velocities from in situ observations at temperatures from 0° to -86°C, *J. Atmos. Sci.,* **70,** 4123–4154, doi:10.1175/JAS-D-12-0124.1.

Hu, Y., McFarquhar, G. M., Wu, W., Huang, Y., Schwarzenboeck, A., Protat, A., Korolev, A., Rauber, R. M., and Wang, H., 2021: Dependence of Ice Microphysical Properties on Environmental Parameters: Results from HAIC-HIWC Cayenne Field Campaign. *J. Atmos. Sci.,* **78,** 2957-2981, https://doi.org/10.1175/JAS-D-21-0015.1

Huang, Y., Y. Wang, L. Xue, X. Wei, L. Zhang, H. Li, 2020: Comparison of Three Microphysics Parameterization Schemes in the WRF Model for an Extreme Rainfall Event in the Coastal Metropolitan City of Guangzhou, China. *Atmos. Res.,* **240,** 104939.https://doi.org/10.1016/j.atmosres.2020.104939.

Huang, Y., Wu, W., McFarquhar, G. M., Wang, X., Morrison, H., Ryzhkov, A., Hu, Y., Wolde, M., Nguyen, C., Schwarzenboeck, A., Milbrandt, J., Korolev, A. V., and Heckman, I.: Microphysical processes producing high ice water contents (HIWCs) in tropical convective clouds during the HAIC-HIWC field campaign: evaluation of simulations using bulk microphysical schemes, *Atmos. Chem. Phys.,* **21,** 6919–6944, https://doi.org/10.5194/acp-21-6919-2021, 2021.

Jackson, R. C., G. M. McFarquhar, J. Stith, M. Beals, R. A. Shaw, J. Jensen, J. Fugal, and A. Korolev, 2014: An assessment of the impact of antishattering tips and artifact removal techniques on cloud ice size distributions measured by the 2D cloud probe. *J. Atmos. Oceanic Technol.,* **31,** 2567–2590, doi:10.1175/ JTECH-D-13-00239.1.

Jackson, R. C., G. M. McFarquhar, A. M. Fridlind, and R. Atlas, 2015: The dependence of cirrus gamma size distributions expressed as volumes in N0-λ-μ phase space and bulk cloud properties on environmental conditions: Results from the Small Ice Particles in Cirrus Experiment (SPARTICUS), *J. Geophys. Res. Atmos.,* **120,** 10,351–10,377, doi:10.1002/ 2015JD023492.

Jakob, C., and S. A. Klein, 1999: The role of vertically varying cloud fraction in the parametrization of microphysical processes in the ECMWF model, *Quart. J. Roy. Meteor. Soc.,* **125,** 941–965, doi:10.1002/qj.49712555510.

Jensen, E. J., Lawson, P., Baker, B., Pilson, B., Mo, Q., Heymsfield, A. J., Bansemer, A., Bui, T. P., McGill, M., Hlavka, D., Heymsfield, G., Platnick, S., Arnold, G. T., and Tanelli, S., 2009: On the importance of small ice crystals in tropical anvil cirrus, *Atmos. Chem. Phys.,* **9,** 5519–5537, https://doi.org/10.5194/acp-9- 5519-2009.

Jorgensen, D.P., E.J. Zipser, M.A. LeMone, 1985: Vertical motions in intense hurricanes. *J. Atmos. Sci.,* **42,** 839-856.

Korolev, A., and Isaac, G. A., 2006: Relative humidity in liquid, mixed-phase, and ice clouds. Journal of the atmospheric sciences, 63(11), 2865-2880.

Korolev A V, Emery E F, Strapp J W, et al.,2011: Small ice particles in tropospheric clouds: Fact or artifact? Airborne Icing Instrumentation Evaluation Experiment. *Bull. Amer. Meteor. Soc.,* **92,** 967-973.

Korolev, A. V., Emery, E. F., Strapp, J. W., Cober, S. G., and Isaac, G. A., 2013: Quantification of the effects of shattering on airborne ice particle measurements. *J. Atmos. Oceanic Technol.,* **30,** 2527-2553.

Korolev A V, A. Shashkov, and H. Barker, 2014: Calibrations and performance of the airborne cloud extinction probe. *J. Atmos. Oceanic Technol.,* **31,** 326–345, doi:10.1175/ JTECH-D-13-00020.1.

Korolev, A., and P. Field, 2015: Assessment of the performance of the inter-arrival time algorithm to identify ice shattering artifacts in cloud particle probe measurements. *Atmos. Meas. Tech.,* **8,** 761–777, doi:10.5194/amt-8-761-2015.

Korolev, A., Heckman, I., and Wolde, M., 2018: Observation of Phase Composition and Humidity in: Oceanic Mesoscale Convective Systems, 15th AMS Cloud Physics Conference, Vancouver, BC, 9–13 July 2018, available at: https://ams.confex.com/ams/15CLOUD15ATRAD/webprogram/Paper347111.html.

Lance, S., C. A. Brock, D. Rogers, and J. A. Gordon, 2010: Water droplet calibration of the Cloud Droplet Probe (CDP) and in- flight performance in liquid, ice and mixed-phase clouds during ARCPAC. *Atmos. Meas. Tech.,* **3,** 1683–1706, doi:10.5194/ amt-3-1683-2010.

Lawson, R. P., E. Jensen, D. L. Mitchell, B. Barker, Q. Mo, and B. Pilson, 2010: Microphysical and radiative properties of tropical clouds investigated in TC4 and NAMMA. *J. Geophys. Res.,* **115,** D00J08, https://doi.org/10.1029/2009JD013017.

Leary, C. A., and Houze, R. A., Jr., 1980: The Contribution of Mesoscale Motions to the Mass and Heat Fluxes of an Intense Tropical Convective System. *J. Atmos. Sci.,* **37,** 784-796, https://doi.org/10.1175/1520-0469(1980)037<0784:TCOMMT>2.0.CO;2

Leroy, D., Coutris, P., Emmanuel, F., Schwarzenboeck, A., Strapp, J. W., Lilie, L. E., Korolev, A., McFarquhar, G., Dezitter. F., and Grandin, A., 2016a: HAIC/HIWC field campaigns-Specific findings on ice crystals characteristics in high ice water content cloud regions. In *8th AIAA Atmospheric and Space Environments Conference* (p. 4056). [Available online at https://doi.org/10.2514/6.2016-4056.]

Leroy, D., E. Fontaine, A. Schwarzenboeck, and J. W. Strapp, 2016b: Ice crystal sizes in high ice water content clouds. Part I: On the computation of median mass diameters from in situ measurements. *J. Atmos. Oceanic Technol.,* **33,** 2461–2476, doi:10.1175/JTECH-D-15-0151.1.

Leroy, D., E. Fontaine, A. Schwarzenboeck, J.W. Strapp, A. Korolev, G. McFarquhar, R. Dupuy, C. Gourbeyre, L. Lilie, A. Protat, J. Delanoë, F. Dezitter, and A. Grandin, 2017: Ice crystal sizes in high ice water content clouds. Part 2: Median Mass Diameter Statistics in Tropical Convection observed during the HAIC/HIWC project, *J. Atmos. Ocean. Tech.*, **34,** 117-136.

Li, X. and Pu, Z., 2008: Sensitivity of numerical simulation of early rapid intensification of

Hurricane Emily (2005) to cloud microphysical and planetary boundary layer parameterizations. *Mon. Wea. Rev.,* **136,** 4819–4838.

Lin, Y. and B.A. Colle, 2011: A new bulk microphysical scheme that includes riming intensity and temperature-dependent ice characteristics. *Mon. Wea. Rev.,* **139,** 1013-1035.

Locatelli, J. D., and P. V. Hobbs, 1974: Fall speeds and masses of solid precipitation particles. *J. Geophys. Res.,* **79,** 2185–2197, doi:10.1029/JC079i015p02185.

Lucas, C., E. J. Zipser, and M. A. Lemone, 1994: Vertical velocity in oceanic convection off tropical Australia. *J. Atmos. Sci.,* **51,** 3183–3193, doi:10.1175/15200469(1994)051,3183:VVIOCO.2.0.CO;2.

Machado, L. A. T., and W. B. Rossow, 1993: Structural characteristics and radiative properties of tropical cloud clusters. *Mon. Wea. Rev.,* **121,** 3234–3260.

Mascio, J., McFarquhar, G. M., Hsieh, T. L., Freer, M., Dooley, A., and Heymsfield, A. J., 2020: The use of gamma distributions to quantify the dependence of cloud particle size distributions in hurricanes on cloud and environmental conditions. *Quart. J. Roy. Meteor. Soc.,* **146,** 2116-2137.

Matsui, T., J. Chern, W. Tao, S. Lang, M. Satoh, T. Hashino, and T. Kubota, 2016: On the Land–Ocean Contrast of Tropical Convection and Microphysics Statistics Derived from TRMM Satellite Signals and Global Storm-Resolving Models. *J. Hydrometeor.,* **17,** 1425–1445, https://doi.org/10.1175/JHM-D-15-0111.1.

Mazin, I. P., Korolev, A. V., Heymsfield, A., Isaac, G. A., and Cober, S. G., 2001: Thermodynamics of icing cylinder for measurements of liquid water content in supercooled clouds. *J. Atmos. Oceanic Technol.,* **18,** 543-558.

McCumber, M., W. K. Tao, J. Simpson, R. Penc, and S. T. Soong, 1991: Comparison of ice-phase microphysical parameterization schemes using numerical simulations of tropical convection. *J. Appl. Meteor.,* **30,** 985–1004, doi:10.1175/ 1520-0450-30.7.985.

McFarquhar, G. M., and A. J. Heymsfield, 1996: Microphysical characteristics of three anvils sampled during the Central Equatorial Pacific Experiment. *J. Atmos. Sci.,* **53,** 2401–2423, doi:10.1175/1520-0469(1996)053,2401: MCOTAS.2.0.CO;2.

McFarquhar, G. M., and Heymsfield, A. J., 1997: Parameterization of tropical cirrus ice crystal size distributions and implications for radiative transfer: Results from CEPEX. *J. Atmos. Sci.*, **54,** 2187-2200.

McFarquhar, G. M., and A. J. Heymsfield, 1998: The definition and significance of an effective radius for ice clouds. *J. Atmos. Sci.,* **55,** 2039–2052, doi:10.1175/ 1520-0469(1998)055,2039:TDASOA.2.0.CO;2.

McFarquhar, G. M., and R. A. Black, 2004: Observations of particle size and phase in tropical cyclones: Implications for meso- scale modeling of microphysical processes. *J. Atmos. Sci.,* **61,** 422–439, doi:10.1175/1520-0469(2004)061,0422: OOPSAP.2.0.CO;2.

McFarquhar, G.M., H. Zhang, G. Heymsfield, R. Hood, J. Dudhia, J.B. Halverson, and F. Marks, 2006: Factors affecting the evolution of Hurricane Erin (2001) and the distributions of hydrometeors: Role of microphysical processes. *J. Atmos. Sci.,* **63,** 127-150.

McFarquhar, G.M., M. S. Timlin, R. M. Rauber, B. F. Jewett, J. A. Grim, and D. P. Jorgensen, 2007: Vertical variability of cloud hydro-meteors in the stratiform region of mesoscale convective systems and bow echoes. *Mon. Wea. Rev.,* **135,** 3405–3428, doi:10.1175/MWR3444.1.

McFarquhar, G. M., Jewett, B. F., Gilmore, M. S., Nesbitt, S. W., and Hsieh, T., 2012: Vertical Velocity and Microphysical Distributions Related to Rapid Intensification in a Simulation of Hurricane Dennis (2005). *J. Atmos. Sci.,* **69,** 3515-3534, https://doi.org/10.1175/JAS-D-12-016.1

McFarquhar, G. M., Hsieh, T. L., Freer, M., Mascio, J., and Jewett, B. F., 2015: The characterization of ice hydrometeor gamma size distributions as volumes in N0–λ–μ phase space: Implications for microphysical process modeling. *J. Atmos. Sci.,* **72,** 892-909.

McFarquhar, G. M., Baumgardner, D., Bansemer, A., Abel, S. J., Crosier, J., French, J., Rosenberg, P., Korolev, A., Schwarzoenboeck, A., Leroy, D., Um, J., Wu, W., Heymsfield, A. J., Twohy, C., Detwiler, A., Field, P., Neumann, A., Cotton, R., Axisa, D., and Dong, J., 2017: Processing of Ice Cloud In Situ Data Collected by Bulk Water, Scattering, and Imaging Probes: Fundamentals, Uncertainties, and Efforts toward Consistency. *Meteor. Monogr.,* **58,** 11.1-11.33, https://doi.org/10.1175/AMSMONOGRAPHS-D-16-0007.1.

Meyers, M. P., R. L. Walko, J. Y. Harrington, and W. R. Cotton, 1997: New RAMS cloud microphysics. Part II: The two-moment scheme. *Atmos. Res.,* **45,** 3–39, doi:10.1016/ S0169-8095(97)00018-5.

Milbrandt, J. A., and M. K. Yau, 2005: A multimoment bulk microphysics parameterization. Part

I: Analysis of the role of the spectral shape parameter. *J. Atmos. Sci.,* **62,** 3051–3064, doi:10.1175/JAS3534.1.

Mitchell, D. L., and W. P. Arnott, 1994: A model predicting the evolution of ice particle size spectra and radiative properties of cirrus clouds. Part II: Dependence of absorption and extinction on ice crystal morphology. *J. Atmos. Sci.,* **51,** 817–832.

Mitchell, D. L., 1996: Use of mass-and area-dimensional power laws for determining precipitation particle terminal velocities. *J. Atmos. Sci.,* **53,** 1710–1723, doi:10.1175/ 1520-0469(1996)053,1710:UOMAAD.2.0.CO;2.

Mitchell, D. L., 2002: Effective diameter in radiation transfer: General definition, applications and limitations, *J. Atmos. Sci.,* **59,** 2330–2346.

Mitchell, D. L., Rasch, P., Ivanova, D., McFarquhar, G., and Nousiainen, T., 2008: Impact of small ice crystal assumptions on ice sedi- mentation rates in cirrus clouds and GCM simulations. *Geophys. Res. Lett.,* **35,** L09806. https://doi.org/10.1029/ 2008GL033552.

Moisseev, D. N., and Chandrasekar, V., 2007: Examination of the μ–Λ relation suggested for drop size distribution parameters. *J. Atmos. Oceanic Technol.,* **24,** 847-855. https://doi.org/10.1175/JTECH2010.1

Morrison, H. and Grabowski, W., 2008: A novel approach for representing ice microphysics in models: description and tests using a kinematic framework, *J. Atmos. Sci.,* **65,** 1528–1548, https://doi.org/10.1175/2007JAS2491.1.

Morrison, H., Thompson, G., and Tatarskii, V., 2009: Impact of cloud microphysics on the development of trailing stratiform precipitation in a simulated squall line: Comparison of one- and two-moment schemes, *Mon. Weather Rev.,* **137,** 991–1007.

Morrison, H. and J.A. Milbrandt, 2015: Parameterization of cloud microphysics based on the predictions of bulk ice particle properties. Part I: Scheme description and idealized tests. *J. Atmos. Sci.,* **72,** 287-311.

Morrison, H., Milbrandt, J. A., Bryan, G. H., Ikeda, K., Tessendorf, S. A., and Thompson, G., 2015: Parameterization of cloud microphysics based on the prediction of bulk ice particle properties. Part II: Case study comparisons with observations and other schemes. *J. Atmos. Sci.,* **72,** 312-339.

Moshtagh, N., 2006: Minimum volume enclosing ellipsoids. Tech. Rep., 9 pp.

[Available online at http://citeseerx.ist.psu.edu/ viewdoc/download?doi510.1.1.116.7691&rep5rep1&type5pdf.]

Murphy, A. M., R. M. Rauber, G. M. McFarquhar, J. A. Finlon, D. M. Plummer, A. A. Rosenow, and B. F. Jewett, 2017: Amicrophysical analysis of elevated convection in the comma head region of continental winter cyclones. *J. Atmos. Sci.,* **74,** 69–91, https://doi.org/10.1175/JAS-D-16-0204.1.

Protat, A., Delanoë, J., Strapp, J. W., Fontaine, E., Leroy, D., Schwarzenboeck, A., Lilie, L., Davison, C., Dezitter, F., Grandin, A., and Weber, M., 2016: The Measured Relationship between Ice Water Content and Cloud Radar Reflectivity in Tropical Convective Clouds. *J. Appl. Meteor. Climatol.,* **55,** 1707-1729, https://doi.org/10.1175/JAMC-D-15-0248.1.

Qu, Z., Barker, H. W., Korolev, A. V., Milbrandt, J. A., Heckman, I., Bélair, S., Leroyer, S., Vaillancourt, P. A., Wolde, M., Schwarzenböck, A., Leroy, D., Strapp, J. W., Cole, J. N. S., Nguyen, L., and Heidinger, A., 2018: Evaluation of a high-resolution numerical weather prediction model's simulated clouds using observations from CloudSat, GOES-13 and in situ aircraft, *Quart. J. Roy. Meteor. Soc.,* **144,** 1681–1694, https://doi.org/10.1002/qj.3318, http://doi.wiley.com/10.1002/qj.3318.

Ratvasky, T.P., Harrah, S. D., Strapp, J. W., Lilie, L.E., Proctor, F.H., Strickland, J. K., Hunt, P. J., Bedka, K. M., Diskins, G. S., Nowak, J. B., Bui, T. V., Bansemer, A., and Dumont, C. J., 2019: Summary of the High Ice Water Content (HIWC) RADAR Flight Campaigns," SAE Technical Paper 2019-01-2025, NASA/TM-2020-220306, 2019, https://doi.org/10.4271/2019-01-2027.

Sanderson, B. M., C. Piani, W. J. Ingram, D. A. Stone, and M. R. Allen, 2008: Towards constraining climate sensitivity by linear analysis of feedback patterns in thousands of perturbed-physics GCM simulations, *Clim. Dyn.,* **30,** 175–190, doi:10.1007/s00382-007-0.

Schlimme, I., Macke, A., and Reichardt, J., 2005: The impact of ice crystal shapes, size distributions, and spatial structures of cirrus clouds on solar radiative fluxes, *J. Atmos. Sci.,* **62,** 2274–2283, https://doi.org/10.1175/JAS3459.1.

Seifert, A., and K. Beheng, 2006: A two-moment cloud micro- physics parameterization for mixed-phase clouds. Part 1: Model description. *Meteor. Atmos. Phys.,* **92,** 45–66, doi:10.1007/s00703-005-0112-4.

Smith, P. L., 1984: Equivalent radar reflectivity factors for snow and ice particles. *J. Climate Appl.*

Meteor., **23,** 1258–1260, doi:10.1175/1520-0450(1984)023,1258:ERRFFS.2.0.CO;2.

Smith, P. L., and Kliche, D. V., 2005: The bias in moment estimators for parameters of drop size distribution functions: Sampling from exponential distributions. *J. Appl. Meteor.,* **44,** 1195-1205.

Smith, P. L., Kliche, D. V., and Johnson, R. W., 2009: The Bias and Error in Moment Estimators for Parameters of Drop Size Distribution Functions: Sampling from Gamma Distributions. *J. Appl. Meteor. Climatol.,* **48,** 2118-2126, https://doi.org/10.1175/2009JAMC2114.1

SPEC, 2011: 2D-S post-processing using 2D-S View Software: User manual, Version 1.1, 48 pp.

Stanford, M. W., Morrison, H., Varble, A., Berner, J., Wu, W., McFarquhar, G., and Milbrandt, J., 2019: Sensitivity of simulated deep convection to a stochastic ice microphysics framework. *Journa of Advances in Modeling Earth Systems*, **11,** 3362-3389. https://doi.org/10.1029/2019MS001730.

Stephens, G. L., 2005: Cloud feedbacks in the climate system: A critical review, *J. Clim.,* **18,** 237–273.

Straka, J. M., and E. R. Mansell, 2005: A bulk microphysics parameterization with multiple ice precipitation categories. *J. Appl. Meteor.,* **44,** 445–466, doi:10.1175/JAM2211.1.

Strapp, J.W., and Coauthors, 2016a: The high ice water content (HIWC) study of deep convective clouds: Science and technical plan. FAA Rep., DOT/FAA/TC-14/31, 105 pp.

Strapp, J.W., L. E. Lilie, T. P. Ratvasky, C. R. Davison, and C. Dumont, 2016b: Isokinetic TWC Evaporator Probe: Development of the IKP2 and performance testing for the HAIC-HIWC Darwin 2014 and Cayenne Field Campaigns. Proc. Eighth AIAA Atmospheric and Space Environments Conf., Washington, DC, American Institute of Aeronautics and Astronautics, AIAA-2016-4059. [Available online at http://arc.aiaa.org/doi/10.2514/6.2016-4059.]

Strapp, J.W., and Coauthors, 2020: An assessment of cloud total water content and particle size from light test campaign measurements in high ice water content, mixed phase/ice crystal icing conditions: Primary in-situ measurements. FAA Rep., AU5 DOT/FAA/TC-18/1, 262 pp.

Strapp, J.W., and Coauthors, 2021: Comparisons of cloud in situ micro- physical properties of deep convective clouds to appendix D/P using data from the high-altitude ice crystals-high ice water content and high ice water content-RADAR I flight campaigns. SAE Int. J. Aerosp., 14, https://doi.org/10.4271/01-14-02-0007.

Thompson, G., Field, P. R., Rasmussen, R. M., and Hall, W. D., 2008: Explicit forecasts of winter precipitation using an improved bulk microphysics scheme. Part II: Implementation of a new snow parameterization, *Mon. Weather Rev.,* **136,** 5095–5115, https://doi.org/10.1175/2008MWR2387.1.

Tian, L., Heymsfield, G. M., Li, L., Heymsfield, A. J., Bansemer, A., Twohy, C. H., and Srivastava, R. C., 2010: A study of cirrus ice particle size distribution using TC4 observations. *J. Atmos. Sci.,* **67,** 195-216.

Van Weverberg, K., van Lipzig, N. P. M., and Delobbe, L., 2011: The Impact of Size Distribution Assumptions in a Bulk One-Moment Microphysics Scheme on Simulated Surface Precipitation and Storm Dynamics during a Low-Topped Supercell Case in Belgium. *Mon. Wea. Rev.,* **139,** 1131-1147, https://doi.org/10.1175/2010MWR3481.1.

Varley, D. J., 1978: Cirrus particle distribution study, Part I. Air Force Geophysical Laboratory Rep. AFGL-TR-78-0192, 71 pp. [Avail- able from Air Force Geophysical Laboratory, Hanscom Air Force Base, MA 01731.]

Walko, R. L., W. R. Cotton, M. P. Meyers, and J. Y. Harrington, 1995: New RAMS cloud microphysics. Part I: The one- moment scheme. *Atmos. Res.,* **38,** 29–62, doi:10.1016/ 0169-8095(94)00087-T.

Wang, Y., 2002: An Explicit Simulation of Tropical Cyclones with a Triply Nested Movable Mesh Primitive Equation Model: TCM3. Part II: Model Refinements and Sensitivity to Cloud Microphysics Parameterization. *Mon. Wea. Rev.,* **130,** 3022-3036, https://doi.org/10.1175/1520-0493(2002)130<3022:AESOTC>2.0.CO;2.

Yost, C.R., K.M. Bedka, P. Minnis, L. Nguyen, J.W. Strapp, R. Palikonda, K. Khlopenkov, D. Spangenberg, W.L. Smith Jr., A. Protat, and J. Delanoe, 2018: A prototype method for diagnosing high ice water content probability using satellite imager data. *Atmos. Meas. Tech.,* **11,** 1615-1637, doi.org/10.5194/amt-11-1615-2018.

Waitz, F., Schnaiter, M., Leisner, T., and Järvinen, E., 2021: PHIPS-HALO: the airborne Particle Habit

Imaging and Polar Scattering probe – Part 3: Single-particle phase discrimination and particle size distribution based on the angular-scattering function, *Atmos. Meas. Tech.,* **14,** 3049–3070, https://doi.org/10.5194/amt-14-3049-2021, 2021.

Welch, R. M., S. K. Cox, and J. M. Davis, 1980: Solar Radiation and Clouds. *Meteor. Monogr.,* No. 39, Amer. Meteor. Soc., 93 pp.

Wolde, M., Nguyen, C., Korolev, A., and Bastian, M., 2016: Characterization of the Pilot X-band radar responses to the HIWC environment during the Cayenne HAIC-HIWC 2015 Campaign, in: 8th AIAA Atmospheric and Space Environments Conference, American Institute of Aeronautics and Astronautics, Washington, D.C., https://doi.org/10.2514/6.2016-4201, http://arc.aiaa.org/doi/10.2514/6.2016-4201.

Wolf, V., Kuhn, T., and Krämer, M., 2019: On the dependence of cirrus parametrizations on the cloud origin. *Geophys. Res. Lett.,* **46,** 12,565–12,571. https://doi.org/10.1029/2019GL083841.

Wong, R. K. W., and N. Chidambaram, 1985: Gamma size distri- bution and stochastic sampling errors. *J. Climate Appl. Meteor.,* **24,** 568–579, doi:10.1175/1520-0450(1985)024,0568: GSDASS.2.0.CO;2.

Wong, R. K. W., N. Chidambaram, L. Cheng, and M. English, 1988: The sampling variations of hailstone size distributions. *J. Appl. Meteor.,* **27,** 254–260, doi:10.1175/1520-0450(1988)027,0254:TSVOHS.2.0.CO;2.

Wu, Wei, and Greg M. McFarquhar, 2016: On the Impacts of Different Definitions of Maximum Dimension for Nonspherical Particles Recorded by 2D Imaging Probes. *J. Atmos. Oceanic Technol.,* **33,** 1057–72.

Wylie, D., D. L. Jackson, W. P. Menzel, and J. J. Bates, 2005: Trends in global cloud cover in two decades of HIRS observations. *J. Climate*, **18,** 3021–3031, doi:10.1175/JCLI3461.1.

Zender, C. S., and Kiehl, J. T., 1997: Sensitivity of climate simulations to radiative effects of tropical anvil structure. *J. Geophys. Res.,* **102,** 23,793–23,803. https://doi.org/10.1029/97JD02009.

Zhao, Y., G. G. Mace, and J. M. Comstock, 2010: The occurrence of particle size distribution bimodality in midlatitude cirrus from ground-based remote sensing data, *J. Atmos. Sci.,* **68,** 1162–1167, doi:10.1175/2010JAS3354.1.

Zhu, T., and Zhang, D., 2006: Numerical Simulation of Hurricane Bonnie (1998). Part II:

Sensitivity to Varying Cloud Microphysical Processes. *J. Atmos. Sci.,* **63,** 1, 109-126, https://doi.org/10.1175/JAS3599.1.

Zipser, E. J., C. Liu, D. J. Cecil, S. W. Nesbitt, and D. P. Yorty, 2006: Where are the most intense thunderstorms on Earth? *Bull. Amer. Meteor. Soc.,* **87,** 1057–1071, doi:10.1175/BAMS-87-8-1057.